Journal of Computational Physics 281 (2015) 493–517

Contents lists available at ScienceDirect

Journal of Computational Physics

www.elsevier.com/locate/jcp

A partitioned scheme for fluid–composite structure interaction problems

M. Bukač [a,*], S. Čanić [b], B. Muha [c]

[a] Department of Applied and Computational Mathematics and Statistics, University of Notre Dame, 158 Hurley Hall, Notre Dame, IN 46556, USA
[b] Department of Mathematics, University of Houston, 4800 Calhoun Rd, Houston, TX 77204, USA
[c] Department of Mathematics, University of Zagreb, Bijenička 30, 10000 Zagreb, Croatia

ARTICLE INFO

Article history:
Received 17 November 2013
Received in revised form 17 October 2014
Accepted 21 October 2014
Available online 24 October 2014

Keywords:
Fluid–structure interaction
Composite structure
Partitioned scheme
Blood flow

ABSTRACT

We present a benchmark problem and a loosely-coupled partitioned scheme for fluid–structure interaction with composite structures. The benchmark problem consists of an incompressible, viscous fluid interacting with a structure composed of two layers: a thin elastic layer with mass which is in contact with the fluid and modeled by the Koiter membrane/shell equations, and a thick elastic layer with mass modeled by the equations of linear elasticity. An efficient, modular, partitioned operator-splitting scheme is proposed to simulate solutions to the coupled, nonlinear FSI problem, without the need for sub-iterations at every time-step. An energy estimate associated with unconditional stability is derived for the fully nonlinear FSI problem defined on moving domains. Two instructive numerical benchmark problems are presented to test the performance of numerical FSI schemes involving composite structures. It is shown numerically that the proposed scheme is at least first-order accurate both in time and space. This work reveals a new physical property of FSI problems involving thin interfaces with mass: the inertia of the thin fluid–structure interface regularizes solutions to the full FSI problem.

1. Introduction

Composite materials are materials made from two or more constituent materials with different physical properties that when combined, produce a material with characteristics different from the individual components [75]. The new material may be preferred for many reasons: common examples include materials which are stronger, lighter or less expensive when compared to traditional materials. Composite materials have been used in virtually all areas of engineering. Examples include marine structures such as boats, ships, and offshore structures, in aerospace industry such as aircraft design, in the design of wind and marine turbines, and in the design of sports' equipment such as skis and tennis racquets. They also appear everywhere in nature. Examples include bones, horns, wood, and biological tissues such as blood vessels of major human arteries. These materials are exposed to a wide spectrum of dynamic loads. In marine structures, aerospace industry, and in many biological constructs, wether natural or man-made, the dynamic loading comes from the surrounding fluid such as water, air, or blood flow. Understanding the interaction between composite materials and the surrounding fluid is important for the understanding of the normal function of the coupled fluid–structure system, as well as the detection

* Corresponding author.
E-mail addresses: mbukac@nd.edu (M. Bukač), canic@math.uh.edu (S. Čanić), borism@math.hr (B. Muha).

http://dx.doi.org/10.1016/j.jcp.2014.10.045
0021-9991/

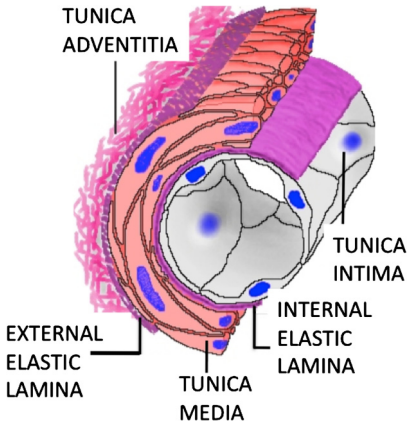

Fig. 1. Arterial wall layers.

of damage and/or pathologies in their function. Prevention of catastrophic events in engineered constructs, or the design of medical treatments to prevent further biological tissue damage, is aided by computational and experimental studies of fluid–composite structure interaction.

In problems in which the fluid and structure have comparable densities, which is the case with most biological tissues (e.g., arterial walls and blood), or in problems in which the structure density is less than the density of water, which is the case in several sandwich composite materials immersed in water [46], the exchange in energy between the fluid and structure is so significant that classical Dirichlet–Neumann loosely-coupled partitioned schemes for numerical simulation of these kinds of problems are unconditionally unstable [15,56]. This is due to the so called added mass effect, also known as virtual mass, or hydrodynamic mass. As the structure vibrates, its mass is increased by the mass of the surrounding fluid, consequently decreasing its natural frequency. This is due to the increase of total kinetic energy of the structure and fluid from the addition of the kinetic energy of the fluid, which significantly impacts the structure vibrations when the structure is "light" relative to the fluid. A comprehensive study of these problems remains to be a challenge due to their significant energy exchange leading to strong nonlinearities in the coupled FSI problem, and due to the intrinsic multi-physics nature of the problem.

The motivation for this paper comes from fluid–structure interaction between blood flow and cardiovascular tissue. Arterial walls of major human arteries are composite materials consisting of three main layers: the intima, media and adventitia, separated by thin elastic laminae, see Fig. 1. Arterial walls interact with blood flow. This interaction plays a crucial role in the normal physiology and pathophysiology of the human cardiovascular system.

In medium-to-large human arteries, such as the aorta or coronary arteries, blood can be modeled as an incompressible, viscous, Newtonian fluid. Due to the fact that density of blood is comparable to that of arterial wall tissue, the corresponding fluid–structure interaction problem suffers from the added mass effect, discussed above. Except for the Immersed Boundary Method approaches, to this date, there have been no FSI numerical solvers based on the Arbitrary Lagrangian–Eulerian approaches, that would take into account the multi-layered structure of arterial walls, and the full nonlinear (two-way) coupling with blood flow. In this manuscript we take a first step in this direction by proposing to study a benchmark problem in fluid–multi-layered-structure interaction in which the structure consists of two layers, a thin and a thick layer, where the thin layer serves as a fluid–structure interface with mass. The thin layer is modeled by the cylindrical Koiter membrane equations, while the thick layer by the equations of linear elasticity. The proposed problem is a nonlinear moving-boundary problem of parabolic–hyperbolic type.

Our computational method is based on an operator-splitting approach, introduced in [62] to study the existence of solutions to an associated fluid–multi-layered structure interaction problem. To achieve stability and convergence, the splitting is performed in a special way in which the fluid sub-problem includes the thin structure inertia via a "Robin-type" boundary condition. The fact that the thin structure inertia is included implicitly in the fluid sub-problem, gives rise to the appropriate energy estimates for the approximate solutions, independent of the size of the time discretization, that provide unconditional stability of the underlying scheme. A couple of numerical examples are presented showing convergence and stability of the scheme. Although the benchmark problem and numerical examples are given in 2D, there is nothing in the methodology that depends on the spatial dimension. An application of the splitting to a problem in 3D can be found in [63], where a FSI with a single thin structure was considered.

The work presented in this manuscript reveals a *new physical phenomenon* which is related to the smoothing effects provided by the purely elastic fluid–structure interface *with mass*. The computational results presented in Example 2 of this manuscript show that the fluid–structure interface inertia regularizes the motion of the fluid–structure interface, and provides a new regularizing mechanism for solutions of FSI problems involving interfaces with mass.

1.1. Literature review

The development of numerical solvers for fluid–structure interaction problems has become particularly active since the 1980's [67,68,22,30,51,47,35,34,37,36,19,41,40,48,50,70,69,3,72,20,23,44,45,16,29].

Until recently, only monolithic algorithms seemed applicable to blood flow simulations [29,32,66,77,8,9]. These algorithms are based on solving the entire nonlinear coupled problem as one monolithic system. They are, however, generally quite expensive in terms of computational time, programming time and memory requirements, since they require solving a sequence of strongly coupled problems using, e.g., the fixed point and Newton's methods [52,66,18,24,40,55].

The multi-physics nature of the blood flow problem strongly suggests to employ partitioned (or staggered) numerical algorithms, where the coupled fluid–structure interaction problem is separated into a fluid and a structure sub-problem. The fluid and structure sub-problems are integrated in time in an alternating way, and the coupling conditions are enforced asynchronously. When the density of the structure is much larger than the density of the fluid, as is the case in aeroelasticity, it is sufficient to solve, at every time step, just one fluid sub-problem and one structure sub-problem to obtain a solution. The classical loosely-coupled partitioned schemes of this kind typically use the structure velocity in the fluid sub-problem as Dirichlet data for the fluid velocity (enforcing the no-slip boundary condition at the fluid–structure interface), while in the structure sub-problem the structure is loaded by the fluid normal stress calculated in the fluid sub-problem. These Dirichlet–Neumann loosely-coupled partitioned schemes work well for problems in which the structure is much heavier than the fluid. Unfortunately, when fluid and structure have comparable densities, which is the case in the blood flow application, the simple strategy of separating the fluid from the structure suffers from severe stability issues [15,56] associated with the added mass effect, discussed in the introduction. The added mass effect reflects itself in Dirichlet–Neumann loosely coupled partitioned schemes by having a poor approximation of the total energy of the coupled problem at every time step of the scheme. A partial solution to this problem is to iterate several times between the fluid and structure sub-solvers at every time step until the energy of the continuous problem is well approximated. These strongly-coupled partitioned schemes, however, are computationally expensive and may suffer from convergence issues for certain parameter values [15].

To get around these difficulties, and to retain the main advantages of loosely-coupled partitioned schemes such as modularity, simple implementation, and low computational costs, several new loosely-coupled algorithms have been proposed recently. In general, they behave quite well for FSI problems containing a thin fluid–structure interface with mass [4,10,12,38,66,25,28,26,27,1,2,6,69,64,18,17].

For FSI problem in which the structure is "thick" relative to the fluid, i.e., the thickness of the structure is comparable to the transverse dimension of the fluid domain, partitioned, loosely-coupled schemes are more difficult to construct. In fact, to the best of our knowledge, there have been no loosely-coupled, partitioned schemes proposed so far in literature for a class of FSI problems in hemodynamics that contain thick structure models to study the elastodynamics of arterial walls. The closest works in this direction include a strongly-coupled partition scheme by Badia et al. in [5], a coupled momentum method by Figueroa et al. in [29], an explicit scheme by Burman and Fernández where certain "defect-correction" sub-iterations are necessary to achieve optimal accuracy [14], and an operator-splitting scheme by Bukač et al. [13] where a version of Lie splitting was used to design a modular, "semi-partitioned" scheme.

Recently, a novel loosely coupled partitioned scheme, called the Kinematically Coupled β-Scheme, was introduced by Bukač, Čanić et al. in [10,12], and applied to FSI problems with thin elastic and viscoelastic structures, modeled by the membrane or shell equations. It was shown in [74] that the scheme is unconditionally stable even for the parameters associated with the blood flow applications. Stability is achieved by combining the structure inertia with the fluid sub-problem as a Robin boundary condition, to mimic the energy balance of the continuous, coupled problem, while the structure problem is treated separately. The Robin boundary condition in the fluid sub-problem only depends on the structure thickness and density, in contrast with the coupled momentum method by Figueroa [29], where the whole structure equation is included in the fluid problem, leading to an ill-conditioned system more comparable to the one obtained by a monolithic formulation. Additionally, Muha and Čanić showed that a version of the kinematically-coupled scheme with $\beta = 0$ converges to a weak solution of the fully nonlinear FSI problem [61]. The case $\beta = 0$ considered in [61] corresponds to the classical kinematically-coupled scheme, first introduced in [38]. Parameter β was introduced in [10] to increase the accuracy of the scheme. It was shown in [10] that the accuracy of the kinematically-coupled β-scheme with $\beta = 1$ was comparable to that of monolithic scheme by Badia, Quaini, and Quarteroni in [6] when applied to the nonlinear benchmark FSI problem in hemodynamics, introduced by Formaggia et al. in [31]. A different approach to increasing the accuracy of the classical kinematically-coupled scheme was recently proposed by Fernández et al. [25,28,26]. Their modified kinematically-coupled scheme, called "the incremental displacement-correction scheme" treats the structure displacement explicitly in the fluid sub-step and then corrects it in the structure sub-step. Fernández et al. showed that the accuracy of the incremental displacement-correction scheme is first-order in time. The results were obtained for a FSI problem involving a thin elastic structure.

These recent results indicate that the kinematically-coupled scheme and its modifications provide an appealing way to study multi-physics problems involving FSI. Indeed, due to its simple implementation, modularity, and very good performance, modifications of this scheme have been used by several authors to study different multi-physics problems involving FSI, such as FSI between artery, blood flow, and cardiovascular device called stent [60], FSI with poroelastic structures [11], and FSI involving non-Newtonian fluids [42,53].

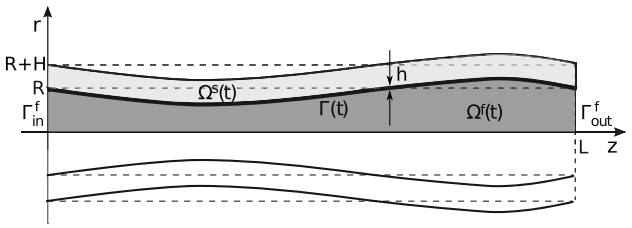

Fig. 2. Deformed domains $\Omega^f(t) \cup \Omega^s(t)$.

The main new results of this manuscript are:

- A benchmark problem is proposed for FSI with composite structures motivated by hemodynamics.
- A fully decoupled, stable kinematically-coupled scheme is designed to study this class of composite FSI problems. The novelty lies in the fact that due to the presence of a thin fluid–structure interface with mass the resulting numerical scheme can be fully decoupled and the fluid and structure sub-problems can be solved on separate domains. This is not the case with FSI problems involving massless interfaces which occurs when only "thick" structures are considered, in which case the fluid sub-problem has to be solved on the union of the fluid and structure domains, which is similar in spirit to monolithic schemes [13].
- For the first time, an energy estimate associated with unconditional stability of a loosely-coupled FSI scheme for the fully nonlinear composite FSI problem is derived (accounting for the fluid advection and fluid–structure coupling at the moving FSI interface with mass).
- A new physical property of FSI problems containing fluid–structure interfaces with mass is discovered: it is shown that interfaces with inertia regularize solutions of FSI problems, giving rise to the structural wave damping not observed in the case of massless interfaces.

2. Description of the fluid–structure interaction problem

We consider the flow of an incompressible, viscous fluid in a two-dimensional channel of reference length L, and reference width $2R$, see Fig. 2. The channel is bounded by a deformable wall, which is composed of two layers: a thin elastic layer with thickness h, and a thick elastic layer with thickness H. The thin layer serves as a fluid–structure interface with mass. We are interested in simulating a pressure-driven flow through the deformable 2D channel with a two-way coupling between the fluid and structure. The structure deforms because of the fluid loading onto the structure, while the fluid flow and the fluid domain are affected by the motion of the elastic structure. Deformation of the structure will be given with respect of a reference configuration, i.e., in Lagrangian framework, where the reference structural domain is assumed to be a uniform cylindrical annulus with constant radius and thickness. Without loss of generality, we consider only the upper half of the fluid domain supplemented by a symmetry condition at the axis of symmetry. Thus, the reference fluid and structure domains in our problem are given, respectively, by

$$\hat{\Omega}^f := \{(z,r) \mid 0 < z < L,\ 0 < r < R\},$$
$$\hat{\Omega}^s := \{(z,r) \mid 0 < z < L,\ R < r < R+H\}.$$

Here z and r denote the horizontal and vertical Cartesian coordinates, respectively (see Fig. 2). The reference configuration of the fluid–structure interface is given by

$$\hat{\Gamma} := \{(z,R) \mid 0 < z < L\}.$$

The flow of an incompressible, viscous fluid is modeled by the Navier–Stokes equations:

$$\rho_f \left(\frac{\partial \boldsymbol{v}}{\partial t} + \boldsymbol{v} \cdot \nabla \boldsymbol{v} \right) = \nabla \cdot \boldsymbol{\sigma}^f(\boldsymbol{v}, p) \quad \text{in } \Omega^f(t) \times (0,T), \tag{1}$$

$$\nabla \cdot \boldsymbol{v} = 0 \quad \text{in } \Omega^f(t) \times (0,T), \tag{2}$$

where $\boldsymbol{v} = (v_z, v_r)$ is the fluid velocity, p is the fluid pressure, ρ_f is fluid density, and $\boldsymbol{\sigma}^f$ is the fluid stress tensor. For a Newtonian fluid the stress tensor is given by $\boldsymbol{\sigma}^f(\boldsymbol{v}, p) = -p\boldsymbol{I} + 2\mu_f \boldsymbol{D}(\boldsymbol{v})$, where μ_f is the fluid viscosity and $\boldsymbol{D}(\boldsymbol{v}) = (\nabla \boldsymbol{v} + (\nabla \boldsymbol{v})^\tau)/2$ is the rate-of-strain tensor.

The inlet to the fluid domain will be denoted by $\Gamma^f_{in} = \{0\} \times (0,R)$, and the outlet by $\Gamma^f_{out} = \{L\} \times (0,R)$. The flow will be driven by the inlet and outlet "pressure" data. Two sets of inlet and outlet boundary conditions will be considered.

BC1. The *normal stress* inlet and outlet data:

$$\boldsymbol{\sigma} \boldsymbol{n}^f_{in/out} = -p_{in/out}(t) \boldsymbol{n}^f_{in/out} \quad \text{on } \Gamma^f_{in/out} \times (0,T), \tag{3}$$

where $\boldsymbol{n}_{in}^f$ and $\boldsymbol{n}_{out}^f$ are the corresponding outward unit normals. Even though not physiologically optimal, these boundary conditions are common in blood flow simulations [4,58,65].

BC2. The *dynamic pressure* inlet and outlet data:

$$\left.\begin{aligned} p + \frac{\rho_f}{2}|u|^2 &= p_{in/out}(t) \\ u_r &= 0 \end{aligned}\right\} \quad \text{on } \Gamma_{in/out}^f \times (0,T), \tag{4}$$

where $p_{in/out} \in L^2_{loc}(0,\infty)$ are given. This set of boundary conditions will be used in energy estimates and in the proof of stability of the proposed scheme.

At the bottom fluid boundary denoted by Γ_b, defined by $(0,L)\times\{0\}$, the following symmetry conditions are prescribed:

$$\frac{\partial v_z}{\partial r}(z,0,t) = 0, \qquad v_r(z,0,t) = 0 \quad \text{on } (0,L)\times(0,T). \tag{5}$$

The lateral fluid boundary is bounded by a deformable, composite structure. The thin layer, which is in contact with the fluid, is modeled by the linearly elastic Koiter membrane model:

$$\rho_m h \frac{\partial^2 \hat{\eta}_z}{\partial t^2} - C_2 \frac{\partial \hat{\eta}_r}{\partial \hat{z}} - C_1 \frac{\partial^2 \hat{\eta}_z}{\partial \hat{z}^2} = \hat{f}_z \quad \text{on } \hat{\Gamma}\times(0,T), \tag{6}$$

$$\rho_m h \frac{\partial^2 \hat{\eta}_r}{\partial t^2} + C_0 \hat{\eta}_r + C_2 \frac{\partial \hat{\eta}_z}{\partial \hat{z}} = \hat{f}_r \qquad \text{on } \hat{\Gamma}\times(0,T), \tag{7}$$

where $\hat{\boldsymbol{\eta}}(\hat{z},t) = (\hat{\eta}_z(\hat{z},t), \hat{\eta}_r(\hat{z},t))$ denotes the axial and radial components of displacement, $\hat{\boldsymbol{f}} = (\hat{f}_z, \hat{f}_r)$ is the surface density of the force applied to the shell, ρ_m denotes membrane density, and

$$C_0 = \frac{h}{R^2}\left(\frac{2\mu_m\lambda_m}{\lambda_m + 2\mu_m} + 2\mu_m\right), \qquad C_1 = h\left(\frac{2\mu_m\lambda_m}{\lambda_m + 2\mu_m} + 2\mu_m\right), \qquad C_2 = \frac{h}{R}\frac{2\mu_m\lambda_m}{\lambda_m + 2\mu_m}, \tag{8}$$

where μ_m and λ_m are the Lamé constants. In terms of the Young's modulus of elasticity and Poisson ratio, coefficients C_0, C_1, and C_2 can be written as

$$C_0 = \frac{hE}{R^2(1-\sigma^2)}, \qquad C_1 = \frac{hE}{1-\sigma^2}, \qquad C_2 = \frac{hE\sigma}{R(1-\sigma^2)}.$$

The thick layer of the wall will be modeled by the equations of linear elasticity with an (artificially) added extra term $\gamma\hat{\mathbf{U}}$, where $\hat{\mathbf{U}}$ denotes the thick structure displacement. This term accounts for the circumferential strain whose effects are lost in the transition from 3D to 2D [4,54,7]. Although γ, in general, should be a matrix (to account for the different stresses in different directions), we take γ to be a scalar, as in [4,54,7], for easier comparison with the available FSI results presented in those publications. The model reads:

$$\rho_s \frac{\partial^2 \hat{\boldsymbol{U}}}{\partial t^2} + \gamma \hat{\boldsymbol{U}} = \nabla\cdot\boldsymbol{\sigma}^s(\hat{\boldsymbol{U}}) \quad \text{in } \hat{\Omega}^s\times(0,T), \tag{9}$$

where $\hat{\boldsymbol{U}} = (\hat{U}_z, \hat{U}_r)$ is the structure displacement and ρ_s is the structure density. We will be assuming that the thick structure behaves as a linearly elastic Saint-Venant Kirchhoff material, in which case the stress–displacement relationship is given by

$$\boldsymbol{\sigma}^s(\hat{\boldsymbol{U}}) = 2\mu_s\boldsymbol{D}(\hat{\boldsymbol{U}}) + \lambda_s(\nabla\cdot\hat{\boldsymbol{U}})\boldsymbol{I},$$

where μ_s and λ_s are the Lamé coefficients for the thick layer. In the simulations presented in Sections 6.1 and 6.2 the Lamé constants of the thin and thick structural layer will be assumed to be the same:

$$\lambda_m = \lambda_s, \qquad \mu_m = \mu_s.$$

The thick structure will be assumed to be fixed at the inlet and outlet boundaries:

$$\hat{\boldsymbol{U}}(0,r,t) = \hat{\boldsymbol{U}}(L,r,t) = 0 \quad \text{on } [R, R+H]\times(0,T). \tag{10}$$

Furthermore, at the external structure boundary $\hat{\Gamma}_{ext}^s = \{R+H\}\times(0,L)$ the structure will be exposed to zero external ambient pressure with zero axial displacement:

$$\boldsymbol{n}_{ext}^s\cdot\boldsymbol{\sigma}^s\boldsymbol{n}_{ext}^s = 0 \quad \text{on } \hat{\Gamma}_{ext}^s\times(0,T), \tag{11}$$

$$\hat{U}_z = 0 \qquad \text{on } \hat{\Gamma}_{ext}^s\times(0,T), \tag{12}$$

where $\boldsymbol{n}_{ext}^s$ is the outward unit normal vector on $\hat{\Gamma}_{ext}^s$.

Initially, the fluid and the structure are assumed to be at rest, with zero displacement from the reference configuration

$$\boldsymbol{v}=0, \qquad \hat{\boldsymbol{\eta}}=0, \qquad \frac{\partial\hat{\boldsymbol{\eta}}}{\partial t}=0, \qquad \hat{\boldsymbol{U}}=0, \qquad \frac{\partial\hat{\boldsymbol{U}}}{\partial t}=0, \quad \text{at } t=0. \tag{13}$$

The fluid and the composite structure are coupled via the following kinematic and dynamic boundary conditions [73,57]:

- **Kinematic coupling conditions** describe continuity of velocity at the fluid–structure interface (no-slip)

$$\boldsymbol{v}\big(\hat{z}+\hat{\eta}_z(\hat{z},t),R+\hat{\eta}_r(\hat{z},t),t\big)=\frac{\partial\hat{\boldsymbol{\eta}}}{\partial t}(\hat{z},t) \quad \text{on } (0,L)\times(0,T), \tag{14}$$

and continuity of displacement

$$\hat{\boldsymbol{\eta}}(\hat{z},t)=\hat{\boldsymbol{U}}(\hat{z},R,t) \quad \text{on } (0,L)\times(0,T); \tag{15}$$

- **Dynamic coupling condition** describes the second Newton's law of motion of the fluid–structure interface, which is loaded by the normal stresses exerted by both the fluid and thick structure. The condition reads:

$$\begin{pmatrix}\rho_m h\frac{\partial^2\hat{\eta}_z}{\partial t^2}-C_2\frac{\partial\hat{\eta}_r}{\partial\hat{z}}-C_1\frac{\partial^2\hat{\eta}_z}{\partial\hat{z}^2}\\ \rho_m h\frac{\partial^2\hat{\eta}_r}{\partial t^2}+C_0\hat{\eta}_r+C_2\frac{\partial\hat{\eta}_z}{\partial\hat{z}}\end{pmatrix}=J\widehat{\boldsymbol{\sigma}^f\boldsymbol{n}^f}\big|_{\Gamma(t)}+\boldsymbol{\sigma}^s\boldsymbol{n}^s\big|_{\hat{\Gamma}}, \tag{16}$$

on $(0,L)\times(0,T)$, where J denotes the Jacobian of the transformation from Eulerian to Lagrangian coordinates, and $\widehat{\boldsymbol{\sigma}^f\boldsymbol{n}^f}|_{\Gamma(t)}$ denotes the normal fluid stress at the deformed fluid–structure interface, evaluated on the reference configuration, namely at the points $(\hat{z}+\hat{\eta}_z(\hat{z},t),R+\hat{\eta}_r(\hat{z},t))$ for $\hat{z}\in(0,L)$ and $t\in(0,T)$. Vector $\boldsymbol{n}^f$ is the outward unit normal to the deformed fluid domain, and $\boldsymbol{n}^s$ is the outward unit normal to the structure domain.

2.1. The energy of the coupled problem

The coupled fluid–composite structure interaction problem (1)–(16) with *dynamic pressure* inlet and outlet data, satisfies the following energy equality:

$$\begin{aligned}&\frac{d}{dt}\Bigg\{\underbrace{\frac{\rho_f}{2}\|\boldsymbol{v}\|^2_{L^2(\Omega^f(t))}+\frac{\rho_m h}{2}\left\|\frac{\partial\hat{\eta}_z}{\partial t}\right\|^2_{L^2(0,L)}+\frac{\rho_m h}{2}\left\|\frac{\partial\hat{\eta}_r}{\partial t}\right\|^2_{L^2(0,L)}+\frac{\rho_s}{2}\left\|\frac{\partial\hat{\boldsymbol{U}}}{\partial t}\right\|^2_{L^2(\hat{\Omega}^s)}}_{\text{Kinetic energy of the coupled problem}}\\ &\underbrace{+h\left[4\mu_m\left\|\frac{\hat{\eta}_r}{R}\right\|^2_{L^2(0,L)}+4\mu_m\left\|\frac{\partial\hat{\eta}_z}{\partial\hat{z}}\right\|^2_{L^2(0,L)}+\frac{4\mu_m\lambda_m}{\lambda_m+2\mu_m}\left\|\frac{\partial\hat{\eta}_z}{\partial\hat{z}}+\frac{\hat{\eta}_r}{R}\right\|^2_{L^2(0,L)}\right]}_{\text{Membrane elastic energy}}\\ &\underbrace{+\frac{\gamma}{2}\|\hat{\boldsymbol{U}}\|^2_{L^2(\hat{\Omega}^s)}+\mu_s\|\boldsymbol{D}(\hat{\boldsymbol{U}})\|^2_{L^2(\hat{\Omega}^s)}+\frac{\lambda_s}{2}\|\nabla\cdot\hat{\boldsymbol{U}}\|^2_{L^2(\hat{\Omega}^s)}}_{\text{Thick structure elastic energy}}\Bigg\}+\underbrace{2\mu_f\|\boldsymbol{D}(\boldsymbol{v})\|^2_{L^2(\Omega^f(t))}}_{\text{Fluid viscous energy}}\\ &=\int_0^R p_{in}(t)v_z\big|_{z=0}dr-\int_0^R p_{out}(t)v_z\big|_{z=L}dr.\end{aligned} \tag{17}$$

The derivation of the energy equality above is similar to that in [62] where the proof of existence of a weak solution to the coupled problem was proved. The energy equality (17) states that if a smooth solution to the coupled fluid–structure interaction problem (1)–(16) exists, then the rate of change of the kinetic energy of the fluid, the kinetic energy of the multilayered structure, and the elastic energy of the structure, plus the viscous dissipation of the fluid, are counter-balanced by the work done by the inlet and outlet data.

2.2. The ALE framework

To circumvent the difficulty associated with the fact that the fluid domain changes in time, we adopt the Arbitrary Lagrangian Eulerian (ALE) method [41,19,65]. The ALE approach is based on introducing a family of arbitrary, smooth, homeomorphic mappings $\mathcal{A}_t$ defined on the reference domain $\hat{\Omega}^f$ such that, for each $t\in(t_0,T)$, $\mathcal{A}_t$ maps the reference domain $\hat{\Omega}^f$ into the current domain $\Omega^f(t)$:

$$\mathcal{A}_t:\hat{\Omega}^f\to\Omega^f(t)\subset\mathbb{R}^2, \qquad \boldsymbol{x}=\mathcal{A}_t(\hat{\boldsymbol{x}})\in\Omega^f(t), \quad \text{for } \hat{\boldsymbol{x}}\in\hat{\Omega}^f.$$

Written in ALE framework, system (1)–(2) reads as follows: Find $\boldsymbol{v}=(v_z,v_r)$ and p, with $\hat{\boldsymbol{v}}(\hat{\boldsymbol{x}},t)=\boldsymbol{v}(\mathcal{A}_t(\hat{\boldsymbol{x}}),t)$ such that

$$\rho_f\left(\left.\frac{\partial \boldsymbol{v}}{\partial t}\right|_{\hat{\boldsymbol{x}}} + (\boldsymbol{v}-\boldsymbol{w})\cdot\nabla\boldsymbol{v}\right) = \nabla\cdot\boldsymbol{\sigma}^f(\boldsymbol{v},p), \quad \text{in } \Omega^f(t)\times(0,T), \tag{18}$$

$$\nabla\cdot\boldsymbol{v} = 0 \quad \text{in } \Omega^f(t)\times(0,T), \tag{19}$$

where $\boldsymbol{w} = \frac{\partial \mathcal{A}_t(\hat{\boldsymbol{x}})}{\partial t}$ denotes the domain velocity. Note that $\frac{\partial f}{\partial t}|_{\hat{\boldsymbol{x}}}$ denotes the time derivative of f evaluated on the reference domain.

2.3. Weak formulation of the coupled FSI problem

For all $t\in[0,T)$ define the following test function spaces

$$V^f(t) = \left\{\boldsymbol{\varphi}:\Omega^f(t)\to\mathbb{R}^2 \;\middle|\; \boldsymbol{\varphi}=\hat{\boldsymbol{\varphi}}\circ(\mathcal{A}_t)^{-1}, \hat{\boldsymbol{\varphi}}\in\left(H^1(\hat{\Omega}^f)\right)^2,\ \varphi_r|_{r=0}=0,\ \boldsymbol{\varphi}|_{z=0,L}=0\right\}, \tag{20}$$

$$Q(t) = \left\{q:\Omega^f(t)\to\mathbb{R} \;\middle|\; q=\hat{q}\circ(\mathcal{A}_t)^{-1}, \hat{q}\in L^2(\hat{\Omega}^f)\right\}, \tag{21}$$

$$\hat{V}^m = \left\{\hat{\boldsymbol{\zeta}}:(0,L)\to\mathbb{R}^2 \;\middle|\; \hat{\boldsymbol{\zeta}}\in\left(H_0^1(\hat{\Gamma})\right)^2\right\}, \tag{22}$$

$$\hat{V}^s = \left\{\hat{\boldsymbol{\psi}}:\hat{\Omega}^s\to\mathbb{R}^2 \;\middle|\; \hat{\boldsymbol{\psi}}\in\left(H^1(\hat{\Omega}^s)\right)^2, \hat{\boldsymbol{\psi}}|_{z=0,L}=0, \hat{\psi}_z|_{\hat{\Gamma}^s_{ext}}=0\right\}, \tag{23}$$

and introduce the function space

$$V^{fsi} = \left\{(\boldsymbol{\varphi},\hat{\boldsymbol{\zeta}},\hat{\boldsymbol{\psi}})\in V^f(t)\times\hat{V}^m\times\hat{V}^s \;\middle|\; \boldsymbol{\varphi}|_{\Gamma(t)}=\boldsymbol{\zeta},\ \hat{\boldsymbol{\zeta}}=\hat{\boldsymbol{\psi}}|_{\hat{\Gamma}}\right\}, \tag{24}$$

where $\boldsymbol{\zeta} := \hat{\boldsymbol{\zeta}}\circ(\mathcal{A}_t^{-1}|_{\Gamma(t)})$. The variational formulation of the coupled fluid–structure interaction problem now reads: given $t\in(0,T)$, find $(\boldsymbol{v},\hat{\boldsymbol{\eta}},\hat{\boldsymbol{U}},p)\in V^f(t)\times\hat{V}^m\times\hat{V}^s\times Q(t)$ such that (14) and (15) hold and such that for all $(\boldsymbol{\varphi},\hat{\boldsymbol{\zeta}},\hat{\boldsymbol{\psi}},q)\in V^{fsi}\times Q(t)$

$$\begin{aligned}
&\rho_f\int_{\Omega^f(t)}\frac{\partial\boldsymbol{v}}{\partial t}\cdot\boldsymbol{\varphi}d\boldsymbol{x} + \int_{\Omega^f(t)}(\boldsymbol{v}\cdot\nabla)\boldsymbol{v}\cdot\boldsymbol{\varphi}d\boldsymbol{x} + 2\mu_f\int_{\Omega^f(t)}\boldsymbol{D}(\boldsymbol{v}):\boldsymbol{D}(\boldsymbol{\varphi})d\boldsymbol{x}\\
&\quad - \int_{\Omega^f(t)}p\nabla\cdot\boldsymbol{\varphi}d\boldsymbol{x} + \int_{\Omega^f(t)}q\nabla\cdot\boldsymbol{v}d\boldsymbol{x} + \rho_m h\int_0^L\frac{\partial^2\hat{\eta}_z}{\partial t^2}\hat{\zeta}_z d\hat{z} + \rho_m h\int_0^L\frac{\partial^2\hat{\eta}_r}{\partial t^2}\hat{\zeta}_r d\hat{z}\\
&\quad - C_2\int_0^L\frac{\partial\hat{\eta}_r}{\partial\hat{z}}\hat{\zeta}_z d\hat{z} + C_1\int_0^L\frac{\partial\hat{\eta}_z}{\partial\hat{z}}\frac{\partial\hat{\zeta}_z}{\partial\hat{z}}d\hat{z} + C_0\int_0^L\hat{\eta}_r\hat{\zeta}_r d\hat{z} + C_2\int_0^L\frac{\partial\hat{\eta}_z}{\partial\hat{z}}\hat{\zeta}_r d\hat{z} + \rho_s\int_{\hat{\Omega}^s}\frac{\partial^2\hat{\boldsymbol{U}}}{\partial t^2}\cdot\boldsymbol{\psi}d\hat{\boldsymbol{x}}\\
&\quad + 2\mu_s\int_{\hat{\Omega}^s}\boldsymbol{D}(\hat{\boldsymbol{U}}):\boldsymbol{D}(\hat{\boldsymbol{\psi}})d\hat{\boldsymbol{x}} + \lambda_s\int_{\hat{\Omega}^s}(\nabla\cdot\hat{\boldsymbol{U}})(\nabla\cdot\hat{\boldsymbol{\psi}})d\hat{\boldsymbol{x}} + \gamma\int_{\hat{\Omega}^s}\hat{\boldsymbol{U}}\cdot\hat{\boldsymbol{\psi}}d\hat{\boldsymbol{x}}\\
&= \int_0^R p_{in}(t)\varphi_z|_{z=0}dr - \int_0^R p_{out}(t)\varphi_z|_{z=L}dr,
\end{aligned} \tag{25}$$

supplemented with initial conditions.

3. The splitting algorithm

To numerically solve the fluid–multilayered structure interaction (1)–(16) we propose a loosely coupled scheme based on the Lie operator splitting algorithm [33].

3.1. The Lie scheme and the first-order system

To apply the Lie splitting scheme the problem must first be written as a first-order system in time:

$$\frac{\partial\phi}{\partial t} + A(\phi) = 0, \quad \text{in } (0,T), \tag{26}$$

$$\phi(0) = \phi_0, \tag{27}$$

where A is an operator from a Hilbert space into itself. Operator A is then split, in a non-trivial decomposition, as

$$A = \sum_{i=1}^{I} A_i. \tag{28}$$

The time discretization via Lie splitting consists of the following. Let $\Delta t > 0$ be a time discretization step. Denote $t^n = n\Delta t$ and let ϕ^n be an approximation of $\phi(t^n)$. Set $\phi^0 = \phi_0$. Then, for $n \geq 0$ compute ϕ^{n+1} by solving

$$\frac{\partial \phi_i}{\partial t} + A_i(\phi_i) = 0 \quad \text{in } \left(t^n, t^{n+1}\right), \tag{29}$$

$$\phi_i\left(t^n\right) = \phi^{n+(i-1)/I}, \tag{30}$$

and then set $\phi^{n+i/I} = \phi_i(t^{n+1})$, for $i = 1, \ldots, I$.

This method is first-order accurate in time. More precisely, if (26) is defined on a finite-dimensional space, and if the operators A_i are smooth enough, then $\|\phi(t^n) - \phi^n\| = O(\Delta t)$ [33]. In our case, operator A that is associated with problem (1)–(16) will be split into a sum of three operators:

A1. The thick structure elastodynamics problem with thin structure elastodynamics included as Robin-type boundary condition.
A2(a). A time-dependent Stokes problem with thin structure inertia included as Robin boundary condition.
A2(b). The fluid advection problem.

Operator A1 defines a structure problem. Operators A2(a) and A2(b) define a fluid problem.

To rewrite system (1)–(16) in first-order form, we introduce two new variables denoting the thin and thick structure velocities:

$$\hat{\boldsymbol{\xi}} = \frac{\partial \hat{\boldsymbol{\eta}}}{\partial t} \quad \text{and} \quad \hat{\boldsymbol{V}} = \frac{\partial \hat{\boldsymbol{U}}}{\partial t}.$$

System (1)–(16) can be written in first-order ALE form as follows: Find $\boldsymbol{v} = (v_z, v_r)$, p, $\hat{\boldsymbol{\eta}} = (\hat{\eta}_z, \hat{\eta}_r)$, $\hat{\boldsymbol{\xi}} = (\hat{\xi}_z, \hat{\xi}_r)$, $\hat{\boldsymbol{U}} = (\hat{U}_z, \hat{U}_r)$ and $\hat{\boldsymbol{V}} = (\hat{V}_z, \hat{V}_r)$, with $\hat{\boldsymbol{v}}(\hat{\boldsymbol{x}}, t) = \boldsymbol{v}(\mathcal{A}_t(\hat{\boldsymbol{x}}), t)$, such that

$$\rho_f \left(\left. \frac{\partial \boldsymbol{v}}{\partial t} \right|_{\hat{\boldsymbol{x}}} + (\boldsymbol{v} - \boldsymbol{w}) \cdot \nabla \boldsymbol{v} \right) = \nabla \cdot \boldsymbol{\sigma}^f(\boldsymbol{v}, p) \quad \text{in } \Omega^f(t) \times (0, T), \tag{31a}$$

$$\nabla \cdot \boldsymbol{v} = 0 \quad \text{in } \Omega^f(t) \times (0, T), \tag{31b}$$

$$\rho_m h \frac{\partial \hat{\xi}_z}{\partial t} - C_2 \frac{\partial \hat{\eta}_r}{\partial \hat{z}} - C_1 \frac{\partial^2 \hat{\eta}_z}{\partial \hat{z}^2} = \hat{f}_z \quad \text{on } \hat{\Gamma} \times (0, T), \tag{31c}$$

$$\rho_m h \frac{\partial \hat{\xi}_r}{\partial t} + C_0 \hat{\eta}_r + C_2 \frac{\partial \hat{\eta}_z}{\partial \hat{z}} = \hat{f}_r \quad \text{on } \hat{\Gamma} \times (0, T), \tag{31d}$$

$$\frac{\partial \hat{\boldsymbol{\eta}}}{\partial t} = \hat{\boldsymbol{\xi}} \quad \text{on } \hat{\Gamma} \times (0, T), \tag{31e}$$

$$\rho_s \frac{\partial \hat{\boldsymbol{V}}}{\partial t} + \gamma \hat{\boldsymbol{U}} = \nabla \cdot \boldsymbol{\sigma}^s(\hat{\boldsymbol{U}}) \quad \text{in } \hat{\Omega}^s \times (0, T), \tag{31f}$$

$$\frac{\partial \hat{\boldsymbol{U}}}{\partial t} = \hat{\boldsymbol{V}} \quad \text{in } \hat{\Omega}^s \times (0, T), \tag{31g}$$

with the following coupling conditions at the fluid–structure interface:

$$\boldsymbol{\xi} = \boldsymbol{v}|_{\Gamma(t)}, \qquad \hat{\boldsymbol{\eta}} = \hat{\boldsymbol{U}}|_{\hat{\Gamma}}, \tag{32}$$

$$\rho_m h \frac{\partial \widehat{(v_z|_{\Gamma(t)})}}{\partial t} - C_2 \frac{\partial \hat{\eta}_r}{\partial \hat{z}} - C_1 \frac{\partial^2 \hat{\eta}_z}{\partial \hat{z}^2} + J \widehat{\boldsymbol{\sigma} \boldsymbol{n}^f|_{\Gamma(t)}} \cdot \boldsymbol{e}_z + \boldsymbol{\sigma}^s \boldsymbol{n}^s|_{\hat{\Gamma}} \cdot \boldsymbol{e}_z = 0, \tag{33}$$

$$\rho_m h \frac{\partial \widehat{(v_r|_{\Gamma(t)})}}{\partial t} + C_0 \hat{\eta}_r + C_2 \frac{\partial \hat{\eta}_z}{\partial \hat{z}} + J \widehat{\boldsymbol{\sigma} \boldsymbol{n}^f|_{\Gamma(t)}} \cdot \boldsymbol{e}_r + \boldsymbol{\sigma}^s \boldsymbol{n}^s|_{\hat{\Gamma}} \cdot \boldsymbol{e}_r = 0. \tag{34}$$

This problem is supplemented with the boundary and initial conditions presented in Section 2.

3.2. Details of the operator-splitting scheme

The following splitting of the fluid stress $\widehat{\boldsymbol{\sigma}^f \boldsymbol{n}^f}$ will be used in the splitting algorithm:

$$\widehat{\boldsymbol{\sigma}^f \boldsymbol{n}^f} = \underbrace{\widehat{\boldsymbol{\sigma}^f \boldsymbol{n}^f} + \beta \widehat{p \boldsymbol{n}^f}}_{(\text{Part I})} \underbrace{- \beta \widehat{p \boldsymbol{n}^f}}_{(\text{Part II})},$$

where $\beta \in [0, 1]$. Part I of the fluid stress will be included in the Robin-type boundary condition for the fluid sub-problem, while Part II of the fluid stress will be included in the Robin-type boundary condition for the thick structure equations. Details of the scheme are as follows.

Problem A1. This problem involves solving the thick structure problem on $\hat{\Omega}_S$, with membrane elastodynamics serving as a Robin-type boundary condition on $\hat{\Gamma}$. The Robin boundary condition also includes Part II of the normal fluid stress, evaluated at the previous time-step, as part of the loading for the elastodynamics of the thin structure.

The problem reads: Find $\boldsymbol{v}$, $\hat{\boldsymbol{\eta}}$, $\hat{\boldsymbol{\xi}}$, $\hat{\boldsymbol{V}}$, and $\hat{\boldsymbol{U}}$, with $\hat{\boldsymbol{v}}(\hat{\boldsymbol{x}},t)=\boldsymbol{v}(\mathcal{A}_t(\hat{\boldsymbol{x}}),t)$ such that:

$$\left.\begin{aligned}&\rho_s\frac{\partial\hat{\boldsymbol{V}}}{\partial t}+\gamma\hat{\boldsymbol{U}}=\nabla\cdot\boldsymbol{\sigma}^s(\hat{\boldsymbol{U}})\\&\frac{\partial\hat{\boldsymbol{U}}}{\partial t}=\hat{\boldsymbol{V}}\end{aligned}\right\}\quad\text{in }\hat{\Omega}^s\times\left(t^n,t^{n+1}\right),\tag{35}$$

satisfying the following conditions on $\hat{\Gamma}\times(t^n,t^{n+1})$:

$$\begin{aligned}&\rho_m h\frac{\partial(\widehat{v_z|_{\Gamma(t)}})}{\partial t}-C_2\frac{\partial\hat{\eta}_r}{\partial\hat{z}}-C_1\frac{\partial^2\hat{\eta}_z}{\partial\hat{z}^2}+\boldsymbol{\sigma}^s\boldsymbol{n}^s|_{\hat{\Gamma}}\cdot\boldsymbol{e}_z=J^n\left(\beta p^n\widehat{\boldsymbol{n}^f|_{\Gamma(t)}}\right)\cdot\boldsymbol{e}_z,\\&\rho_m h\frac{\partial(\widehat{v_r|_{\Gamma(t)}})}{\partial t}+C_0\hat{\eta}_r+C_2\frac{\partial\hat{\eta}_z}{\partial\hat{z}}+\boldsymbol{\sigma}^s\boldsymbol{n}^s|_{\hat{\Gamma}}\cdot\boldsymbol{e}_r=J^n\left(\beta p^n\widehat{\boldsymbol{n}^f|_{\Gamma(t)}}\right)\cdot\boldsymbol{e}_r,\\&\frac{\partial\hat{\boldsymbol{\eta}}}{\partial t}=\hat{\boldsymbol{\xi}},\qquad\boldsymbol{\xi}=\boldsymbol{v}|_{\Gamma(t)},\qquad\hat{\boldsymbol{\eta}}=\hat{\boldsymbol{U}}|_{\hat{\Gamma}},\end{aligned}$$

and satisfying the following boundary conditions at $z=0,L$ and at $\hat{\Gamma}^s_{ext}$:

$$\begin{aligned}&\hat{\boldsymbol{U}}|_{z=0,L}=0,\\&\hat{U}_z=0,\qquad\boldsymbol{n}^s_{ext}\cdot\boldsymbol{\sigma}^s\boldsymbol{n}^s_{ext}=0\quad\text{on }\hat{\Gamma}^s_{ext}\times\left(t^n,t^{n+1}\right).\end{aligned}$$

The initial conditions are given by the values of the unknown functions at the end of the previous time step:

$$\boldsymbol{v}\left(t^n\right)=\boldsymbol{v}^n,\qquad\hat{\boldsymbol{\eta}}\left(t^n\right)=\hat{\boldsymbol{\eta}}^n,\qquad\hat{\boldsymbol{\xi}}\left(t^n\right)=\hat{\boldsymbol{\xi}}^n,\qquad\hat{\boldsymbol{U}}\left(t^n\right)=\hat{\boldsymbol{U}}^n,\qquad\hat{\boldsymbol{V}}\left(t^n\right)=\hat{\boldsymbol{V}}^n.$$

The fluid velocity remains unchanged:

$$\left.\frac{\partial\boldsymbol{v}}{\partial t}\right|_{\hat{\boldsymbol{x}}}=0\quad\text{in }\Omega^f\left(t^n\right)\times\left(t^n,t^{n+1}\right).$$

The values of the just calculated variables are set to be $\boldsymbol{v}^{n+1/3}=\boldsymbol{v}(t^{n+1})$, $\hat{\boldsymbol{\eta}}^{n+1/3}=\hat{\boldsymbol{\eta}}(t^{n+1})$, $\hat{\boldsymbol{\xi}}^{n+1/3}=\hat{\boldsymbol{\xi}}(t^{n+1})$, $\hat{\boldsymbol{U}}^{n+1/3}=\hat{\boldsymbol{U}}(t^{n+1})$, $\hat{\boldsymbol{V}}^{n+1/3}=\hat{\boldsymbol{V}}(t^{n+1})$, $p^{n+1}=p(t^{n+1})$.

Using the just-calculated values of the thin structure displacement and velocity we compute the ALE velocity $\boldsymbol{w}$ by defining $\mathcal{A}_{t^{n+1}}$ to be the harmonic extension of the structure displacement $\hat{\boldsymbol{\eta}}^{n+1/3}$ at the fluid–structure interface onto the whole domain $\hat{\Omega}^f$

$$\begin{aligned}&\Delta\mathcal{A}_{t^{n+1}}=0\quad\text{in }\hat{\Omega}^f,\\&\mathcal{A}_{t^{n+1}}|_{\hat{\Gamma}}=\hat{\boldsymbol{\eta}}^{n+1/3},\\&\mathcal{A}_{t^{n+1}}|_{\partial\hat{\Omega}^f\setminus\hat{\Gamma}}=0.\end{aligned}$$

Then, we define $\boldsymbol{w}^{n+1}=\frac{\partial\mathcal{A}_{t^{n+1}}}{\partial t}=\frac{\partial\boldsymbol{x}}{\partial t}\approx\frac{\boldsymbol{x}^{n+1}-\boldsymbol{x}^n}{\Delta t}$, which remains unchanged in Problems 2(a) and 2(b).

Remark 1. Note that using the kinematic coupling conditions we can rewrite the membrane equations in the following way:

$$\begin{aligned}&\rho_m h\frac{\partial\hat{V}_z}{\partial t}-C_2\frac{\partial\hat{U}_r}{\partial\hat{z}}-C_1\frac{\partial^2\hat{U}_z}{\partial\hat{z}^2}+\boldsymbol{\sigma}^s\boldsymbol{n}^s|_{\hat{\Gamma}}\cdot\boldsymbol{e}_z=J^n\left(\beta p^n\widehat{\boldsymbol{n}^f|_{\Gamma(t)}}\right)\cdot\boldsymbol{e}_z,\quad\text{on }\hat{\Gamma}\times\left(t^n,t^{n+1}\right),\\&\rho_m h\frac{\partial\hat{V}_r}{\partial t}+C_0\hat{U}_r+C_2\frac{\partial\hat{U}_z}{\partial\hat{z}}+\boldsymbol{\sigma}^s\boldsymbol{n}^s|_{\hat{\Gamma}}\cdot\boldsymbol{e}_r=J^n\left(\beta p^n\widehat{\boldsymbol{n}^f|_{\Gamma(t)}}\right)\cdot\boldsymbol{e}_r\qquad\text{on }\hat{\Gamma}\times\left(t^n,t^{n+1}\right).\end{aligned}$$

In this way the membrane equations become a Robin-type boundary condition for the thick structure problem, and Problem A1 becomes a pure structure problem.

Problem A2(a). This problem involves solving a time dependent Stokes problem with a Robin-type boundary condition involving the structure inertia and Part I of the fluid stress. This problem is solved on a fixed fluid domain $\Omega^f(t^n)$, which is determined by the location of the structure position calculated in the previous time step.

The problem reads as follows: Find $\boldsymbol{v}$, p, $\hat{\boldsymbol{\eta}}$, $\hat{\boldsymbol{\xi}}$, $\hat{\boldsymbol{V}}$ and $\hat{\boldsymbol{U}}$, with $\hat{\boldsymbol{v}}(\hat{\boldsymbol{x}},t)=\boldsymbol{v}(\mathcal{A}_t(\hat{\boldsymbol{x}}),t)$ such that for $t\in(t^n,t^{n+1})$, with p^n obtained at the previous time step, the following holds:

$$\left.\begin{aligned} \rho_f \left.\frac{\partial \boldsymbol{v}}{\partial t}\right|_{\hat{\boldsymbol{x}}} &= \nabla \cdot \boldsymbol{\sigma}^f \\ \nabla \cdot \boldsymbol{v} &= 0 \end{aligned}\right\} \quad \text{in } \Omega^f\left(t^n\right) \times \left(t^n, t^{n+1}\right), \tag{36}$$

with the Robin-type boundary condition on $\hat{\Gamma} \times (t^n, t^{n+1})$ given by:

$$\rho_m h \frac{\partial \widehat{(\boldsymbol{v}|_{\Gamma(t)})}}{\partial t} + J\left(\boldsymbol{\sigma}^f \boldsymbol{n}^f\big|_{\Gamma(t)}\widehat{\ } + \beta p^n \widehat{\boldsymbol{n}^f\big|_{\Gamma(t)}}\right) = 0.$$

This is supplemented with the following inlet and outlet boundary conditions on (t^n, t^{n+1}):

$$\boldsymbol{v}(0, R, t) = \boldsymbol{v}(L, R, t) = 0,$$
$$\boldsymbol{\sigma}^f \boldsymbol{n}_{in}^f = -p_{in}(t)\boldsymbol{n}_{in}^f \quad \text{on } \Gamma_{in}^f, \qquad \boldsymbol{\sigma}^f \boldsymbol{n}_{out}^f = -p_{out}(t)\boldsymbol{n}_{out}^f \quad \text{on } \Gamma_{out}^f,$$

and the following symmetry boundary conditions at $r = 0$:

$$\frac{\partial v_z}{\partial r}(z, 0, t) = v_r(z, 0, t) = 0 \quad \text{on } (0, L) \times \left(t^n, t^{n+1}\right).$$

The location of the structure remains unchanged:

$$\frac{\partial \hat{\boldsymbol{\eta}}}{\partial t} = 0 \qquad \text{on } \hat{\Gamma} \times \left(t^n, t^{n+1}\right),$$
$$\frac{\partial \hat{\boldsymbol{V}}}{\partial t} = \frac{\partial \hat{\boldsymbol{U}}}{\partial t} = 0 \quad \text{in } \hat{\Omega}^s \times \left(t^n, t^{n+1}\right).$$

The initial conditions are given by: $\boldsymbol{v}(t^n) = \boldsymbol{v}^{n+1/3}$, $\hat{\boldsymbol{\eta}}(t^n) = \hat{\boldsymbol{\eta}}^{n+1/3}$, $\hat{\boldsymbol{\xi}}(t^n) = \hat{\boldsymbol{\xi}}^{n+1/3}$, $\hat{\boldsymbol{U}}(t^n) = \hat{\boldsymbol{U}}^{n+1/3}$, and $\hat{\boldsymbol{V}}(t^n) = \hat{\boldsymbol{V}}^{n+1/3}$.

After a solution to this problem is calculated, set $\boldsymbol{v}^{n+2/3} = \boldsymbol{v}(t^{n+1})$, $\hat{\boldsymbol{\eta}}^{n+2/3} = \hat{\boldsymbol{\eta}}(t^{n+1})$, $\hat{\boldsymbol{\xi}}^{n+2/3} = \hat{\boldsymbol{\xi}}(t^{n+1})$, $\hat{\boldsymbol{U}}^{n+2/3} = \hat{\boldsymbol{U}}(t^{n+1})$, $\hat{\boldsymbol{V}}^{n+2/3} = \hat{\boldsymbol{V}}(t^{n+1})$, $p^{n+1} = p(t^{n+1})$.

Problem A2(b). Solve the fluid and ALE advection sub-problem defined on the fixed domain $\Omega^f(t^n)$, with the domain velocity $\boldsymbol{w}^{n+1}$ just calculated in Problem A1.

The problem reads: Find $\boldsymbol{v}$, $\hat{\boldsymbol{\eta}}$, $\hat{\boldsymbol{\xi}}$, $\hat{\boldsymbol{V}}$ and $\hat{\boldsymbol{U}}$, with $\hat{\boldsymbol{v}}(\hat{\boldsymbol{x}}, t) = \boldsymbol{v}(\mathcal{A}_t(\hat{\boldsymbol{x}}), t)$ and $\boldsymbol{w}^{n+1}$ computed in Problem A1, such that:

$$\left.\frac{\partial \boldsymbol{v}}{\partial t}\right|_{\hat{\boldsymbol{x}}} + \left(\boldsymbol{v}^n - \boldsymbol{w}^{n+1}\right) \cdot \nabla \boldsymbol{v} = 0 \quad \text{in } \Omega^f\left(t^n\right) \times \left(t^n, t^{n+1}\right),$$

with the lateral boundary condition on $\hat{\Gamma} \times (t^n, t^{n+1})$ given by

$$\rho_m h \frac{\partial \widehat{(\boldsymbol{v}|_{\Gamma(t)})}}{\partial t} = 0,$$

and with the inlet/outlet boundary conditions defined on the portion of the boundary for which the slope of the characteristics associated with the advection problem, defined by the sign of $(\boldsymbol{v}^n - \boldsymbol{w}^{n+1}) \cdot \boldsymbol{n}$, is pointing inward, toward the fluid domain:

$$\boldsymbol{v} = \boldsymbol{v}^{n+2/3}, \quad \text{on } \Gamma_-^{n+2/3}, \text{ where } \Gamma_-^{n+2/3} = \left\{\boldsymbol{x} \in \mathbb{R}^2 \;\middle|\; \boldsymbol{x} \in \partial\Omega^f\left(t^n\right), \left(\boldsymbol{v}^n - \boldsymbol{w}^{n+1}\right) \cdot \boldsymbol{n} < 0\right\}.$$

The structure does not change in this step:

$$\frac{\partial \hat{\boldsymbol{\eta}}}{\partial t} = 0 \qquad \text{on } \hat{\Gamma} \times \left(t^n, t^{n+1}\right),$$
$$\frac{\partial \hat{\boldsymbol{V}}}{\partial t} = \frac{\partial \hat{\boldsymbol{U}}}{\partial t} = 0 \quad \text{in } \hat{\Omega}^s \times \left(t^n, t^{n+1}\right).$$

The initial conditions are given by the solution obtained in Problem A2(a): $\boldsymbol{v}(t^n) = \boldsymbol{v}^{n+2/3}$, $\hat{\boldsymbol{\eta}}(t^n) = \hat{\boldsymbol{\eta}}^{n+2/3}$, $\hat{\boldsymbol{\xi}}(t^n) = \hat{\boldsymbol{\xi}}^{n+2/3}$, $\hat{\boldsymbol{U}}(t^n) = \hat{\boldsymbol{U}}^{n+2/3}$, and $\hat{\boldsymbol{V}}(t^n) = \hat{\boldsymbol{V}}^{n+2/3}$.

Then set $\boldsymbol{v}^{n+1} = \boldsymbol{v}(t^{n+1})$, $\hat{\boldsymbol{\eta}}^{n+1} = \hat{\boldsymbol{\eta}}(t^{n+1})$, $\hat{\boldsymbol{\xi}}^{n+1} = \hat{\boldsymbol{\xi}}(t^{n+1})$, $\hat{\boldsymbol{U}}^{n+1} = \hat{\boldsymbol{U}}(t^{n+1})$, $\hat{\boldsymbol{V}}^{n+1} = \hat{\boldsymbol{V}}(t^{n+1})$.

After this step we update the fluid domain position via

$$\Omega^f\left(t^{n+1}\right) = \mathcal{A}_{t^{n+1}}\left(\hat{\Omega}^f\right).$$

Then set $t^n = t^{n+1}$ and return to Problem A1.

4. The discretized scheme in weak form

The Backward Euler scheme is used to approximate the time derivatives on each (t^{n+1}, t^n), while for the space discretization, we use the finite element method approach, based on a conforming FEM triangulation with maximum triangle diameter k. For this purpose, we define the finite element spaces $V_k^f(t^n) \subset V^f(t^n)$, $Q_k(t^n) \subset Q(t^n)$, $\hat{V}_k^m \subset \hat{V}^m$ and $\hat{V}_k^s \subset \hat{V}^s$, and introduce the following bilinear forms

$$a_f^n(\boldsymbol{v}, \boldsymbol{\varphi}) := 2\mu_f \int_{\Omega^f(t^n)} \boldsymbol{D}(\boldsymbol{v}) : \boldsymbol{D}(\boldsymbol{\varphi}) d\boldsymbol{x},$$

$$b_f^n(p, \boldsymbol{\varphi}) := \int_{\Omega^f(t^n)} p \nabla \cdot \boldsymbol{\varphi} d\boldsymbol{x},$$

$$\hat{a}_m(\hat{\boldsymbol{\eta}}, \hat{\boldsymbol{\xi}}) := C_1 \int_0^L \frac{\partial \hat{\eta}_z}{\partial \hat{z}} \frac{\partial \hat{\xi}_z}{\partial \hat{z}} d\hat{z} + C_0 \int_0^L \hat{\eta}_r \hat{\xi}_r d\hat{z} + C_2 \int_0^L \frac{\partial \hat{\eta}_z}{\partial \hat{z}} \hat{\xi}_r d\hat{z} - C_2 \int_0^L \frac{\partial \hat{\eta}_r}{\partial \hat{z}} \hat{\xi}_z d\hat{z},$$

$$\hat{a}_e(\hat{\boldsymbol{U}}, \hat{\boldsymbol{\psi}}) := 2\mu_s \int_{\hat{\Omega}^s} \boldsymbol{D}(\hat{\boldsymbol{U}}) : \boldsymbol{D}(\hat{\boldsymbol{\psi}}) d\hat{\boldsymbol{x}} + \lambda_s \int_{\hat{\Omega}^s} (\nabla \cdot \hat{\boldsymbol{U}})(\nabla \cdot \hat{\boldsymbol{\psi}}) d\hat{\boldsymbol{x}} + \gamma \int_{\hat{\Omega}^s} \hat{\boldsymbol{U}} \cdot \hat{\boldsymbol{\psi}} d\hat{\boldsymbol{x}}.$$

Discretization of the operator splitting scheme discussed above, in weak form, is given by the following:

Problem A1 *(The structure problem).* To discretize the structure problem in time we use the second order Newmark scheme. The problem reads as follows: Find $(\hat{\boldsymbol{U}}_k^{n+1/3}, \hat{\boldsymbol{V}}_k^{n+1/3}) \in \hat{V}_h^s \times \hat{V}_k^s$ such that for all $(\hat{\boldsymbol{\psi}}_k, \hat{\boldsymbol{\phi}}_k) \in \hat{V}_k^s \times \hat{V}_k^s$

$$\begin{aligned}
&\rho_s \int_{\hat{\Omega}^s} \frac{\hat{\boldsymbol{V}}_k^{n+1/3} - \hat{\boldsymbol{V}}_k^n}{\Delta t} \cdot \hat{\boldsymbol{\psi}}_k d\hat{\boldsymbol{x}} + \gamma \int_{\hat{\Omega}^s} \frac{\hat{\boldsymbol{U}}_k^n + \hat{\boldsymbol{U}}_k^{n+1/3}}{2} \cdot \hat{\boldsymbol{\psi}}_k d\hat{\boldsymbol{x}} \\
&\quad + \rho_m h \int_0^L \frac{\hat{\boldsymbol{V}}_k^{n+1/3} - \hat{\boldsymbol{V}}_k^n}{\Delta t} \cdot \hat{\boldsymbol{\psi}}_k d\hat{z} + \hat{a}_m\left(\frac{\hat{\boldsymbol{U}}_k^n + \hat{\boldsymbol{U}}_k^{n+1/3}}{2}, \hat{\boldsymbol{\psi}}_k\right) + \hat{a}_e\left(\frac{\hat{\boldsymbol{U}}_k^n + \hat{\boldsymbol{U}}_k^{n+1/3}}{2}, \hat{\boldsymbol{\psi}}_k\right) \\
&\quad + \rho_s \int_{\hat{\Omega}^s} \left(\frac{\hat{\boldsymbol{V}}_k^n + \hat{\boldsymbol{V}}_k^{n+1/3}}{2} - \frac{\hat{\boldsymbol{U}}_k^{n+1/3} - \hat{\boldsymbol{U}}_k^n}{\Delta t}\right) \cdot \hat{\boldsymbol{\phi}}_k d\hat{\boldsymbol{x}} + \rho_m h \int_0^L \left(\frac{\hat{\boldsymbol{V}}_k^n + \hat{\boldsymbol{V}}_k^{n+1/3}}{2} - \frac{\hat{\boldsymbol{U}}_k^{n+1/3} - \hat{\boldsymbol{U}}_k^n}{\Delta t}\right) \cdot \hat{\boldsymbol{\phi}}_k d\hat{z} \\
&= \int_0^L J^n \beta p^n \widehat{\boldsymbol{n}^f|_{\Gamma(t)}} \cdot \hat{\boldsymbol{\psi}}_k d\hat{z}.
\end{aligned} \tag{37}$$

Note that in this step we take all the kinematic coupling conditions into account: initially we set $\hat{\boldsymbol{V}}_k^n|_\Gamma = \hat{\boldsymbol{\xi}}_k^n = \widehat{\boldsymbol{v}_k^n|_{\Gamma(t^n)}}$; then, once $\hat{\boldsymbol{U}}_k^{n+1/3}$ and $\hat{\boldsymbol{V}}_k^{n+1/3}$ are computed, $\hat{\boldsymbol{\eta}}_k^{n+1/3}$, $\hat{\boldsymbol{\xi}}_k^{n+1/3}$ and $\widehat{\boldsymbol{v}_k^{n+1/3}|_{\Gamma(t^n)}}$ can be recovered via $\hat{\boldsymbol{\eta}}_k^{n+1/3} = \hat{\boldsymbol{U}}_k^{n+1/3}|_\Gamma$ and $\hat{\boldsymbol{\xi}}_k^{n+1/3} = \widehat{\boldsymbol{v}_k^{n+1/3}|_{\Gamma(t^n)}} = \hat{\boldsymbol{V}}_k^{n+1/3}|_\Gamma$.

In this step $\partial \boldsymbol{v}_k / \partial t = 0$, and so $\boldsymbol{v}_k^{n+1/3} = \boldsymbol{v}_k^n$.

At the end of this step we compute the new fluid domain velocity by finding $\mathcal{A}_{t^{n+1}} \in (H^1(\hat{\Omega}^f))^2$ with $\mathcal{A}_{t^{n+1}}|_{\hat{\Gamma}} = \hat{\boldsymbol{\eta}}^{n+1/3}$ and $\mathcal{A}_{t^{n+1}}|_{\partial\hat{\Omega}^f \setminus \hat{\Gamma}} = 0$, such that

$$\int_{\hat{\Omega}^f} \nabla \mathcal{A}_{t^{n+1}} \cdot \nabla \boldsymbol{\zeta} d\hat{\boldsymbol{x}} = 0, \quad \forall \boldsymbol{\zeta} \in \left(H_0^1(\hat{\Omega}^f)\right)^2. \tag{38}$$

Then, the new fluid domain velocity is given by

$$\boldsymbol{w}^{n+1} = \frac{\partial \mathcal{A}_{t^{n+1}}}{\partial t} \approx \frac{\mathcal{A}_{t^{n+1}}(\hat{\boldsymbol{x}}) - \boldsymbol{x}^n}{\Delta t}.$$

Problem A2(a) *(The time dependent Stokes problem).* We discretize Problem A2(a) using the Backward Euler scheme, giving rise to the following weak formulation: Find $(\boldsymbol{v}_k^{n+2/3}, p_k^{n+1}) \in V_k^f(t^n) \times Q_k(t^n)$ such that for all $(\boldsymbol{\varphi}_k, q_k) \in V_k^f(t^n) \times Q_k(t^n)$

$$\rho_f \int_{\Omega^f(t^n)} \frac{\boldsymbol{v}_k^{n+2/3} - \boldsymbol{v}_k^{n+1/3}}{\Delta t} \cdot \boldsymbol{\varphi}_k d\boldsymbol{x} + a_f^n\left(\boldsymbol{v}_k^{n+2/3}, \boldsymbol{\varphi}_k\right) - b_f^n\left(p_k^{n+1}, \boldsymbol{\varphi}_k\right)$$
$$+ b_f^n\left(q_k, \boldsymbol{v}_k^{n+2/3}\right) + \rho_m h \int_0^L \frac{\widehat{\boldsymbol{v}_k^{n+2/3}|_{\Gamma(t^n)}} - \widehat{\boldsymbol{v}_k^{n+1/3}|_{\Gamma(t^n)}}}{\Delta t} \cdot \hat{\boldsymbol{\varphi}}_k d\hat{x}$$
$$= \int_0^R p_{in}\left(t^{n+1}\right)\varphi_{z,k}|_{z=0} dr - \int_0^R p_{out}\left(t^{n+1}\right)\varphi_{z,k}|_{z=L} dr - \int_0^L J^n \beta \widehat{p^n \boldsymbol{n}^f|_{\Gamma(t)}} \cdot \hat{\boldsymbol{\varphi}}_k d\hat{x}. \tag{39}$$

In this step the structure is not moving, and so $\hat{\boldsymbol{U}}_k^{n+2/3} = \hat{\boldsymbol{U}}_k^{n+1/3}$, $\hat{\boldsymbol{V}}_k^{n+2/3} = \hat{\boldsymbol{V}}_k^{n+1/3}$, $\hat{\eta}_k^{n+2/3} = \hat{\eta}_k^{n+1/3}$, and $\hat{\xi}_k^{n+2/3} = \hat{\xi}_k^{n+1/3}$.

Problem A2(b) *(The fluid and ALE advection).* As in the previous step, we discretize Problem A2(b) using the Backward Euler scheme. The weak formulation reads as follows: Find $\boldsymbol{v}_k^{n+1} \in V_k^f(t^n)$ with $\boldsymbol{v}_k^{n+1} = \boldsymbol{v}_k^{n+2/3}$ on $\Gamma_-^{n+2/3}$, such that for all $\boldsymbol{\varphi}_k \in \{\boldsymbol{\varphi}_k \in V_k^f(t^n) \mid \boldsymbol{\varphi}_k = 0 \text{ on } \Gamma_-^{n+2/3}\}$

$$\rho_f \int_{\Omega^f(t^n)} \frac{\boldsymbol{v}_k^{n+1} - \boldsymbol{v}_k^{n+2/3}}{\Delta t} \cdot \boldsymbol{\varphi}_k d\boldsymbol{x} + \rho_f \int_{\Omega^f(t^n)} \left(\left(\boldsymbol{v}_k^n - \boldsymbol{w}_k^{n+1}\right) \cdot \nabla\right) \boldsymbol{v}_k^{n+1} \cdot \boldsymbol{\varphi}_k = 0. \tag{40}$$

Note that here we use $\boldsymbol{w}_k^{n+1}$ computed at the very end of Problem A1.

In this step the structure is not moving, and so

$$\hat{\boldsymbol{U}}_k^{n+1} = \hat{\boldsymbol{U}}_k^{n+2/3}, \qquad \hat{\boldsymbol{V}}_k^{n+1} = \hat{\boldsymbol{V}}_k^{n+2/3}, \qquad \hat{\eta}_k^{n+1} = \hat{\eta}_k^{n+2/3}, \qquad \hat{\xi}_k^{n+1} = \hat{\xi}_k^{n+2/3}.$$

Finally, we update the fluid domain position via

$$\Omega^f\left(t^{n+1}\right) = (\boldsymbol{I} + \mathcal{A}_{t^{n+1}})\left(\hat{\Omega}^f\right).$$

Then, set $t^n = t^{n+1}$ and return to Problem A1.

5. Unconditional stability of the scheme with $\beta = 0$

We show an energy estimate that is associated with unconditional stability of the scheme when $\beta = 0$. In contrast with similar results appearing in literature which consider simplified models without fluid advection, and/or linearized fluid–structure coupling calculated at a fixed fluid domain boundary [15,74,26,14], in this manuscript we prove the desired energy estimate for the full, nonlinear FSI problem, that includes both fluid advection and nonlinear coupling at the moving fluid–structure interface.

To simplify analysis, the following assumptions which do not influence stability of the scheme will be considered:

1. Only radial displacement of the fluid–structure interface is allowed, i.e., $\eta_z = U_z|_{\hat{\Gamma}} = 0$. In that case, we consider the following equation for the radial membrane displacement

$$\rho_m h \frac{\partial^2 \hat{\eta}_r}{\partial t^2} + C_0 \hat{\eta}_r = \hat{f}_r. \tag{41}$$

   The FSI problem with this boundary condition and no "inlet and outlet" displacement boundary conditions is well-defined.
2. The problem is driven by the dynamic inlet and outlet pressure data, and the flow enters and leaves the fluid domain parallel to the horizontal axis:

$$p + \frac{\rho_f}{2}|\boldsymbol{v}|^2 = p_{in/out}(t), \qquad v_r = 0, \quad \text{on } \Gamma_{in/out}^f.$$

To simplify matters, instead of splitting the Navier–Stokes equations into the time dependent Stokes problem and the advection problem, we keep the fluid problem uncoupled so that our splitting scheme becomes:

A1. The thick structure problem involving the membrane elastodynamics equation as a Robin-type boundary condition.
A2. The fluid problem modeled by the Navier–Stokes equations in ALE form, with structure inertia included as a Robin boundary condition for the fluid problem.

5.1. Discretized scheme in weak form assuming only radial displacement of the fluid–structure interface and $\beta = 0$

We introduce the following bilinear form $\hat{a}_m$ associated with the thin structure elastodynamics problem (41):

$$\hat{a}_m(\hat{\eta}_r, \hat{\zeta}_r) = C_0 \int_0^L \hat{\eta}_r \hat{\zeta}_r d\hat{z}.$$

With this notation, the two steps of the discretization scheme can be written as follows:

Problem A1 *(Structure).* Find $(\hat{\boldsymbol{U}}_k^{n+1/2}, \hat{\boldsymbol{V}}_k^{n+1/2}) \in \hat{V}_k^s \times \hat{V}_k^s$ such that for all $(\hat{\boldsymbol{\psi}}_k, \hat{\boldsymbol{\phi}}_k) \in \hat{V}_k^s \times \hat{V}_k^s$

$$\begin{aligned}
&\rho_s \int_{\hat{\Omega}^s} \frac{\hat{\boldsymbol{V}}_k^{n+1/2} - \hat{\boldsymbol{V}}_k^n}{\Delta t} \cdot \hat{\boldsymbol{\psi}}_k d\hat{\boldsymbol{x}} + \gamma \int_{\hat{\Omega}^s} \frac{\hat{\boldsymbol{U}}_k^n + \hat{\boldsymbol{U}}_k^{n+1/2}}{2} \cdot \hat{\boldsymbol{\psi}}_k d\hat{\boldsymbol{x}} \\
&\quad + \rho_m h \int_\Gamma \frac{\hat{V}_{r,k}^{n+1/2} - \hat{V}_{r,k}^n}{\Delta t} \hat{\psi}_{r,k} + \hat{a}_m\left(\frac{\hat{U}_{r,k}^n + \hat{U}_{r,k}^{n+1/2}}{2}, \hat{\psi}_{r,k}\right) + \hat{a}_e\left(\frac{\hat{\boldsymbol{U}}_k^n + \hat{\boldsymbol{U}}_k^{n+1/2}}{2}, \hat{\boldsymbol{\psi}}_k\right) \\
&\quad + \rho_s \int_{\hat{\Omega}^s} \left(\frac{\hat{\boldsymbol{V}}_k^n + \hat{\boldsymbol{V}}_k^{n+1/2}}{2} - \frac{\hat{\boldsymbol{U}}_k^{n+1/2} - \hat{\boldsymbol{U}}_k^n}{\Delta t}\right) \cdot \hat{\boldsymbol{\phi}}_k d\hat{\boldsymbol{x}} + \rho_m h \int_\Gamma \left(\frac{\hat{V}_{r,k}^n + \hat{V}_{r,k}^{n+1/2}}{2} - \frac{\hat{U}_{r,k}^{n+1/2} - \hat{U}_{r,k}^n}{\Delta t}\right) \cdot \hat{\phi}_{r,k} d\hat{z} \\
&= 0,
\end{aligned} \tag{42}$$

with the initial data such that $\hat{V}_{r,k}^n|_\Gamma = \hat{\xi}_{r,k}^n = \widehat{v_{r,k}^n|_{\Gamma(t^n)}}$.

Then set $\hat{\eta}_{r,k}^{n+1/2} = \hat{U}_{r,k}^{n+1/2}|_\Gamma$ and $\hat{\xi}_{r,k}^{n+1/2} = \widehat{v_{r,k}^{n+1/2}|_{\Gamma(t^n)}} = \hat{V}_{r,k}^{n+1/2}|_\Gamma$, and, since the fluid velocity does not change, $\boldsymbol{v}_k^{n+1/2} = \boldsymbol{v}_k^n$.

Problem A2 *(Fluid).* Find $(\boldsymbol{v}_k^{n+1}, p_k^{n+1}) \in V_k^f(t^n) \times Q_k(t^n)$ such that for all $(\boldsymbol{\varphi}_k, q_k) \in V_k^f(t^{n+1}) \times Q_k(t^n)$:

$$\begin{aligned}
&\rho_f \int_{\Omega^f(t^n)} \frac{\boldsymbol{v}_k^{n+1} - \boldsymbol{v}_k^{n+1/2}}{\Delta t} \cdot \boldsymbol{\varphi}_k d\boldsymbol{x} + \frac{\rho_f}{2} \int_{\Omega^f(t^n)} \left(\nabla \cdot \boldsymbol{w}_k^{n+1}\right) \boldsymbol{v}_k^{n+1} \cdot \boldsymbol{\varphi}_k d\boldsymbol{x} \\
&\quad + \frac{\rho_f}{2} \int_{\Omega^f(t^n)} \left(\left(\left(\boldsymbol{v}_k^n - \boldsymbol{w}_k^{n+1}\right) \cdot \nabla\right) \boldsymbol{v}_k^{n+1} \cdot \boldsymbol{\varphi}_k - \left(\left(\boldsymbol{v}_k^n - \boldsymbol{w}_k^{n+1}\right) \cdot \nabla\right) \boldsymbol{\varphi}_k \cdot \boldsymbol{v}_k^{n+1}\right) \\
&\quad + a_f^n\left(\boldsymbol{v}_k^{n+1}, \boldsymbol{\varphi}_k\right) - b_f^n\left(p_k^{n+1}, \boldsymbol{\varphi}_k\right) + b_f^n\left(q_k, \boldsymbol{v}_k^{n+1}\right) + \rho_m h \int_0^L \frac{\widehat{v_{r,k}^{n+1}|_{\Gamma(t^n)}} - \widehat{v_{r,k}^{n+1/2}|_{\Gamma(t^n)}}}{\Delta t} \varphi_{r,k} dx \\
&= \int_0^R p_{in}\left(t^{n+1}\right) \varphi_{z,k}|_{z=0} dr - \int_0^R p_{out}\left(t^{n+1}\right) \varphi_{z,k}|_{z=L} dr,
\end{aligned} \tag{43}$$

where the initial data for the trace of the fluid velocity on $\Gamma(t^n)$ comes from the just calculated velocity of the thin structure $\widehat{v_{r,k}^{n+1/2}|_{\Gamma(t^n)}} = \hat{\xi}_{r,k}^{n+1/2}$.

Then set $\hat{\boldsymbol{U}}_k^{n+1} = \hat{\boldsymbol{U}}_k^{n+1/2}$, $\hat{\boldsymbol{V}}_k^{n+1} = \hat{\boldsymbol{V}}_k^{n+1/2}$, $\hat{\eta}_{r,k}^{n+1} = \hat{\eta}_{r,k}^{n+1/2}$, and $\hat{\xi}_{r,k}^{n+1} = \hat{\xi}_{r,k}^{n+1/2}$.

The ALE velocity $\boldsymbol{w}^{n+1}$ that appears in Problem A2 is calculated after computing the new structure displacement in Problem A1. To update the position of the fluid domain (after Problem A2), we consider the following simple ALE mapping:

$$A_{t^n} : \hat{\Omega}^f \to \Omega^f\left(t^n\right), \qquad A_{t^n}(\hat{z}, \hat{r}) := \left(\hat{z}, \frac{R + \hat{\eta}_{r,k}^n}{R} \hat{r}\right)^\tau.$$

We will also need the explicit form of the ALE mapping from the computational domain $\Omega^f(t^n)$ to $\Omega^f(t^{n+1})$, which is given by

$$A_{t^{n+1}} \circ A_{t^n}^{-1} : \Omega^f\left(t^n\right) \to \Omega^f\left(t^{n+1}\right), \qquad A_{t^{n+1}} \circ A_{t^n}^{-1}(z, r) = \left(z, \frac{R + \hat{\eta}_{r,k}^{n+1}}{R + \hat{\eta}_{r,k}^{n}} r\right)^{\tau}.$$

The corresponding Jacobian and the ALE velocity are given, respectively, by

$$J_n^{n+1} := \frac{R + \hat{\eta}_{r,k}^{n+1}}{R + \hat{\eta}_{r,k}^{n}}, \qquad \boldsymbol{w}_k^{n+1} = \frac{1}{\Delta t} \frac{\hat{\eta}_{r,k}^{n+1} - \hat{\eta}_{r,k}^{n}}{R + \hat{\eta}_{r,k}^{n}} r \boldsymbol{e}_r. \tag{44}$$

Therefore, the time-derivative of the interface displacement is approximated by $(\hat{\eta}_{r,k}^{n+1} - \hat{\eta}_{r,k}^{n})/\Delta t$, which enters the expression for the ALE velocity $\boldsymbol{w}^{n+1}$. This will be used in the stability analysis presented next.

5.2. Stability analysis

Let $\mathcal{E}_f^n$ denote the discrete energy of the fluid problem, $\mathcal{E}_s^n$ the discrete energy of the structure problem, and let $\mathcal{E}_m^n$ denote the discrete energy of the simplified membrane problem at time level $n\Delta t$:

$$\begin{aligned}
\mathcal{E}_f^n &:= \frac{\rho_f}{2} \left\| \boldsymbol{v}_k^n \right\|^2_{L^2(\Omega^f(t^n))}, \\
\mathcal{E}_s^n &:= \frac{\rho_s}{2} \left\| \hat{\boldsymbol{V}}_k^n \right\|^2_{L^2(\hat{\Omega}^s)} + \mu_s \left\| D\left(\hat{\boldsymbol{U}}_k^n\right) \right\|^2_{L^2(\hat{\Omega}^s)} + \frac{\lambda_s}{2} \left\| \nabla \cdot \hat{\boldsymbol{U}}_k^n \right\|^2_{L^2(\hat{\Omega}^s)} + \frac{\gamma}{2} \left\| \hat{\boldsymbol{U}}_k^n \right\|^2_{L^2(\hat{\Omega}^s)}, \\
\mathcal{E}_m^n &:= \frac{\rho_m h}{2} \left\| \hat{\xi}_{r,k}^n \right\|^2_{L^2(0,L)} + \frac{C_0}{2} \left\| \hat{\eta}_{r,k}^n \right\|^2_{L^2(0,L)}.
\end{aligned}$$

Theorem 1 *(An energy estimate of the operator splitting scheme). Let* $\{(\boldsymbol{v}^n, \boldsymbol{U}^n, \boldsymbol{V}^n, \eta_r^n, \xi_r^n)\}_{0 \le n \le N}$ *be a solution of* (42)–(43)*. Then, the following energy estimate holds:*

$$\begin{aligned}
&\mathcal{E}_f^N + \mathcal{E}_s^N + \mathcal{E}_m^N + \frac{\rho_f}{2} \sum_{n=0}^{N-1} \left\| \boldsymbol{v}_k^{n+1} - \boldsymbol{v}_k^{n+1/2} \right\|^2_{L^2(\Omega^f(t^n))} + \mu_f \Delta t \sum_{n=0}^{N-1} \left\| D\left(\boldsymbol{v}_k^{n+1}\right) \right\|^2_{L^2(\Omega^f(t^n))} \\
&\quad + \frac{\rho_m h}{2} \sum_{n=0}^{N-1} \left\| \widehat{v_{r,k}^{n+1}|_{\Gamma(t^n)}} - \widehat{v_{r,k}^{n+1/2}|_{\Gamma(t^n)}} \right\|^2_{L^2(0,L)} \\
&\le \mathcal{E}_f^0 + \mathcal{E}_s^0 + \mathcal{E}_m^0 + \frac{C}{\mu_f} \Delta t \sum_{n=0}^{N-1} \left\| p_{in}\left(t^n\right) \right\|^2_{L^2(0,R)} + \frac{C}{\mu_f} \Delta t \sum_{n=0}^{N-1} \left\| p_{out}\left(t^n\right) \right\|^2_{L^2(0,R)}.
\end{aligned}$$

This energy estimate shows that the total energy of the coupled discretized problem is bounded by the energy of the initial data, and by the work done by the inlet and outlet dynamic pressure data, independently of the time step, for all the parameters in the problem.

Proof. To prove the energy estimate, we test the structure problem (42) with $(\hat{\boldsymbol{\psi}}_k, \hat{\boldsymbol{\phi}}_k) = (\frac{\hat{\boldsymbol{U}}_k^{n+1/2} - \hat{\boldsymbol{U}}_k^n}{\Delta t}, \frac{\hat{\boldsymbol{V}}_k^{n+1/2} - \hat{\boldsymbol{V}}_k^n}{\Delta t})$, and the fluid problem (43) with $(\boldsymbol{\varphi}_k, q_k) = (\boldsymbol{v}_k^{n+1}, p_k^{n+1})$. With this choice of test functions, after multiplying by Δt, Problem A1 reduces to

$$\mathcal{E}_s^{n+1/2} + \frac{\rho_m h}{2} \left\| \hat{\xi}_{r,k}^{n+1/2} \right\|^2_{L^2(0,L)} - \frac{\rho_m h}{2} \left\| \hat{\xi}_{r,k}^{n} \right\|^2_{L^2(0,L)} + \frac{C_0}{2} \left\| \hat{\eta}_{r,k}^{n+1/2} \right\|^2_{L^2(0,L)} - \frac{C_0}{2} \left\| \hat{\eta}_{r,k}^{n} \right\|^2_{L^2(0,L)} = \mathcal{E}_s^n. \tag{45}$$

In Problem A2, after replacing the test functions by the fluid velocity $\boldsymbol{v}_k^{n+1}$, the symmetrized advection terms cancel out. To deal with the first term on the left in Problem A2, we use the identity

$$a(a-b) = \frac{1}{2}\left(a^2 - b^2 + (a-b)^2\right). \tag{46}$$

Then, the first two terms combined (fluid inertia) become

$$\begin{aligned}
&\frac{\rho_f}{2} \frac{1}{\Delta t} \int_{\Omega^f(t^n)} \left(\left(1 + \frac{\hat{\eta}_{r,k}^{n+1} - \hat{\eta}_{r,k}^{n}}{R + \hat{\eta}_{r,k}^{n}} \right) \left| \boldsymbol{v}_k^{n+1} \right|^2 + \left| \boldsymbol{v}_k^{n+1} - \boldsymbol{v}_k^{n+1/2} \right|^2 - \left| \boldsymbol{v}_k^{n+1/2} \right|^2 \right) d\boldsymbol{x} \\
&\quad = \frac{\rho_f}{2} \frac{1}{\Delta t} \int_{\Omega^f(t^n)} \left(\frac{R + \hat{\eta}_{r,k}^{n+1}}{R + \hat{\eta}_{r,k}^{n}} \left| \boldsymbol{v}_k^{n+1} \right|^2 + \left| \boldsymbol{v}_k^{n+1} - \boldsymbol{v}_k^{n+1/2} \right|^2 - \left| \boldsymbol{v}_k^{n+1/2} \right|^2 \right) d\boldsymbol{x}.
\end{aligned}$$

Note that since the fluid does not change in Problem A1, $\boldsymbol{v}_k^{n+1/2} = \boldsymbol{v}_k^n$. Furthermore, notice that $(R+\eta^{n+1})/(R+\eta^n)$ is exactly the Jacobian of the ALE mapping from $\Omega^f(t^n)$ to $\Omega^f(t^{n+1})$, see (44), and so we can convert that integral into an integral over $\Omega^f(t^{n+1})$ to recover the kinetic energy of the fluid at the next time-step:

$$\frac{\rho_f}{2}\frac{1}{\Delta t}\int\limits_{\Omega^f(t^n)}\frac{R+\hat{\eta}_{r,k}^{n+1}}{R+\hat{\eta}_{r,k}^{n}}\left|\boldsymbol{v}_k^{n+1}\right|^2 d\boldsymbol{x} = \frac{\rho_f}{2}\frac{1}{\Delta t}\int\limits_{\Omega^f(t^{n+1})}\left|\boldsymbol{v}_k^{n+1}\right|^2 d\boldsymbol{x}.$$

This calculation also shows that the ALE mapping and its Jacobian satisfy the geometric conservation law property, as studied by Farhat et al. in [21].

Therefore, after multiplying by Δt, the energy associated with Problem A2 is given by

$$\begin{aligned}
&\frac{\rho_f}{2}\left\|\boldsymbol{v}_k^{n+1}\right\|^2_{L^2(\Omega^f(t^{n+1}))} - \frac{\rho_f}{2}\left\|\boldsymbol{v}_k^{n+1/2}\right\|^2_{L^2(\Omega^f(t^n))} + \frac{\rho_f}{2}\left\|\boldsymbol{v}_k^{n+1}-\boldsymbol{v}_k^{n+1/2}\right\|^2_{L^2(\Omega^f(t^n))}\\
&\quad + 2\mu_f\Delta t\left\|D\left(\boldsymbol{v}_k^{n+1}\right)\right\|^2_{L^2(\Omega^f(t^n))} + \frac{\rho_m h}{2}\left\|\widehat{v_{r,k}^{n+1}|_{\Gamma(t^n)}}\right\|^2_{L^2(0,L)} - \frac{\rho_m h}{2}\left\|\widehat{v_{r,k}^{n+1/2}|_{\Gamma(t^n)}}\right\|^2_{L^2(0,L)}\\
&\quad + \frac{\rho_m h}{2}\left\|\widehat{v_{r,k}^{n+1}|_{\Gamma(t^n)}} - \widehat{v_{r,k}^{n+1/2}|_{\Gamma(t^n)}}\right\|^2_{L^2(0,L)}\\
&= \Delta t\int\limits_0^R p_{in}\left(t^{n+1}\right)v_{z,k}^{n+1}|_{z=0}dr - \Delta t\int\limits_0^R p_{out}\left(t^{n+1}\right)v_{z,k}^{n+1}|_{z=L}dr.
\end{aligned}\tag{47}$$

Now, Eqs. (45) and (47) are added, and the following properties are taken into account: first $\widehat{v_{r,k}^{n+1/2}|_{\Gamma(t^n)}} = \hat{\xi}_{r,k}^{n+1/2}$, and further, due to the kinematic coupling condition we also have $\widehat{v_{r,k}^{n+1}|_{\Gamma(t^n)}} = \hat{\xi}_{r,k}^{n+1}$. After adding Eqs. (45) and (47), and taking into account $\mathcal{E}_s^{n+1/2} = \mathcal{E}_s^{n+1}$ since the displacement changes only in the first step, we get

$$\begin{aligned}
&\mathcal{E}_f^{n+1} + \mathcal{E}_s^{n+1} + \mathcal{E}_m^{n+1} + \frac{\rho_f}{2}\left\|\boldsymbol{v}_k^{n+1}-\boldsymbol{v}_k^{n+1/2}\right\|^2_{L^2(\Omega^f(t^n))} + 2\mu_f\Delta t\left\|D\left(\boldsymbol{v}_k^{n+1}\right)\right\|^2_{L^2(\Omega^f(t^n))}\\
&\quad + \frac{\rho_m h}{2}\left\|\widehat{v_{r,k}^{n+1}|_{\Gamma(t^n)}} - \widehat{v_{r,k}^{n+1/2}|_{\Gamma(t^n)}}\right\|^2_{L^2(0,L)}\\
&= \mathcal{E}_f^{n} + \mathcal{E}_s^{n} + \mathcal{E}_m^{n} + \Delta t\int\limits_0^R p_{in}\left(t^{n+1}\right)v_{z,k}^{n+1}|_{z=0}dr - \Delta t\int\limits_0^R p_{out}\left(t^{n+1}\right)v_{z,k}^{n+1}|_{z=L}dr.
\end{aligned}$$

To bound the right-hand side of this equality, we use the Cauchy–Schwartz and Young's inequalities

$$\begin{aligned}
&\Delta t\int\limits_0^R p_{in}\left(t^{n+1}\right)v_{z,k}^{n+1}|_{z=0}dr - \Delta t\int\limits_0^R p_{out}\left(t^{n+1}\right)v_{z,k}^{n+1}|_{z=L}dr\\
&\le \frac{\Delta t}{2\epsilon_1}\left\|p_{in}\left(t^n\right)\right\|^2_{L^2(0,R)} + \frac{\Delta t}{2\epsilon_1}\left\|p_{out}\left(t^n\right)\right\|^2_{L^2(0,R)} + \epsilon_1\Delta t\left\|\boldsymbol{v}_k^{n+1}\right\|^2_{L^2(0,R)}.
\end{aligned}$$

By the trace and Korn inequalities, we then have

$$\left\|\boldsymbol{v}_k^{n+1}\right\|^2_{L^2(0,R)} \le C\left\|\boldsymbol{D}\left(\boldsymbol{v}_k^{n+1}\right)\right\|^2_{L^2(\Omega^f(t^n))},$$

where C is the constant from the trace and Korn inequalities. In general, Korn's constant depends on the domain. It was shown, however, that for domains associated with fluid–structure interaction problems of the type studied in this manuscript, the Korn's constant is independent of the sequence of approximating domains [61,62].

By setting $\epsilon_1 = \frac{\mu_f}{C}$, the last term can be combined with the term on the left hand-side, associated with the fluid diffusion. Finally, summing the inequality from $n=0$ to $N-1$ we prove the desired energy estimate. □

The energy estimate, presented above, shows that the combined linear discretized sub-problems are stable, and that the sequence of approximate solutions to the nonlinear FSI problem is uniformly bounded in the corresponding energy norms.

6. Numerical results

To validate our numerical solver, we present two benchmark problems. In the first example a simplified FSI benchmark problem with a composite structure is designed for which a steady-state analytical solution is found. The problem is solved

Table 1
Geometry, fluid and structure parameters used in Example 1.

Parameters	Values	Parameters	Values
Radius R (cm)	0.5	Length L (cm)	6
In. press. p_{in} (dyne/cm^2)	250	Out. press. p_{out} (dyne/cm^2)	0
Fluid density ρ_f (g/cm^3)	1	Dyn. viscosity μ (g/cm s)	0.035
Thin wall:			
Density ρ_m (g/cm^3)	1.1	Thickness h (cm)	0.02
Lamé coeff. μ_m (dyne/cm^2)	1.07×10^6	Lamé coeff. λ_m (dyne/cm^2)	4.29×10^6
Thick wall:			
Density ρ_s (g/cm^3)	1.1	Thickness H (cm)	0.1
Lamé coeff. μ_s (dyne/cm^2)	1.07×10^6	Lamé coeff. λ_s (dyne/cm^2)	4.29×10^6
Spring coeff. γ (dyne/cm^4)	0		

with the initial data "far away" from the steady-state solution. As $t \to \infty$ it is shown that the numerical solution converges to the analytical steady-state solution.

In the second example the fully nonlinear FSI benchmark problem is considered. However, since there are no benchmark problems in literature which can be used to compare our solution with, we consider a sequence of problems as the thickness h of the thin structure converges to zero, and compare the limiting solution with the known FSI solution involving only a thick structure, showing excellent agreement. On this example both temporal and spatial convergence are studied, showing 1st-order accuracy for the case $\beta = 1$.

6.1. Numerical Example 1: a simplified FSI problem with exact solution

We present a simple FSI problem with multiple structural layers which has an exact solution, and can be used for the testing of FSI solvers with composite structures. The following simplifying assumptions are considered:

1. The fluid problem is defined on the fixed, reference domain of width R, and length L (the FSI coupling is linear).
2. The fluid problem is driven by the constant inlet and outlet pressure data p_{in} and $p_{out} = 0$ (the pressure drop is constant).
3. Only radial displacement of the thin and thick structure is assumed to be different from zero.

Assumption 3 implies that the thin structure membrane model takes the form:

$$\rho_K h \frac{\partial^2 \eta_r}{\partial t} + C_0 \eta_r = f_r,$$

while the thick structure problem simplifies as follows:

$$\rho_s \frac{\partial^2 d_r}{\partial t^2} = \mu \frac{\partial^2 d_r}{\partial x^2} + (\mu + \lambda) \frac{\partial^2 d_r}{\partial y^2}.$$

Finally, the coupling conditions between the fluid and the multilayered structure are given by

$$f_r = p + (\lambda + \mu) \frac{\partial d_r}{\partial y}, \qquad \eta_r = d_r, \qquad \frac{\partial \eta_r}{\partial t} = u_r, \qquad u_z = 0 \quad \text{on } \Gamma \times (0, T).$$

The exact solution to this problem is given by the following. The fluid flow through the fixed cylinder with constant pressure drop is given by the Poiseuille velocity profile:

$$u_z^e(z, r) = u_z^e(r) = \frac{p_{in} - p_{out}}{2\mu_F L}\left(R^2 - r^2\right), \qquad u_r^e = 0,$$

and the fluid pressure is linear within the channel:

$$p^e(z, r) = p^e(z) = \frac{p_{out} z + p_{in}(L - z)}{L}, \quad z \in (0, L),\ r \in (0, R).$$

The radial displacements of the thin and thick structure are given by:

$$\eta_r^e(z) = \frac{p^e(z)}{C_0}, \qquad d_r^e(z, r) = d_r^e(z) = \eta_r^e(z).$$

We solved this problem numerically using the parameters given in Table 1. The corresponding (local) Reynold's number based on the cylinder radius is $Re = \rho R U/\mu = 214$. The initial data was taken far away from the steady state:

$$\mathbf{u} = 0, \qquad p = p_{out}, \qquad \eta_r = 0, \qquad d_r = 0, \quad \text{at } t = 0,$$

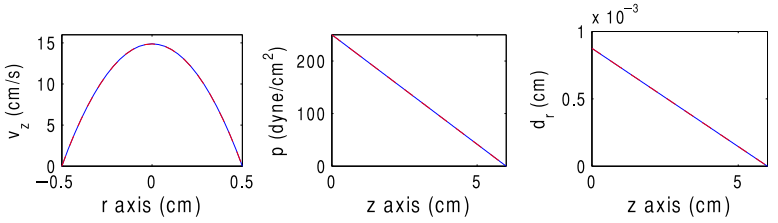

Fig. 3. Comparison between the computed solution (in blue) and the exact solution (in red). The two are superimposed. Left: axial velocity. Middle: fluid pressure. Right: radial displacement. (For interpretation of the references to color in this figure legend, the reader is referred to the web version of this article.)

Table 2
Geometry, fluid and structure parameters that are used in Example 2.

Parameters	Values	Parameters	Values
Radius R (cm)	0.5	Length L (cm)	6
Fluid density ρ_f (g/cm^3)	1	Dyn. viscosity μ (g/cm s)	0.035
Thin wall:			
Density ρ_m (g/cm^3)	1.1	Thickness h (cm)	0.02
Lamé coeff. μ_m (dyne/cm^2)	5.75×10^5	Lamé coeff. λ_m (dyne/cm^2)	1.7×10^6
Thick wall:			
Density ρ_s (g/cm^3)	1.1	Thickness H (cm)	0.1
Lamé coeff. μ_s (dyne/cm^2)	5.75×10^5	Lamé coeff. λ_s (dyne/cm^2)	1.7×10^6
Spring coeff. γ (dyne/cm^4)	4×10^6		

and the flow was driven by the constant inlet and outlet pressure data p_{in} and p_{out}. At the inlet and outlet of the domain, the thin and thick structure displacement were set to:

$$\eta_r|_{z=0} = d_r|_{z=0} = \frac{p_{in}}{C_0}, \qquad \eta_r|_{z=L} = d_r|_{z=L} = \frac{p_{out}}{C_0} = 0, \quad \forall t > 0.$$

The time-dependent problem was solved until the steady state was achieved.

The numerical scheme with $\beta = 1$ was implemented. For the spatial discretization of the fluid problem we again used the P1-iso-P2 elements with a coarse mesh for the pressure (mesh size Δx_p) and a fine mesh for the velocity ($\Delta x_v = \Delta x_p/2$). The problem was solved on a mesh containing 341×15 fluid nodes. For the structure problem, we used P1 elements on a mesh containing 341×7 nodes. With the time step $\Delta t = 10^{-5}$ it took 200 iterations to achieve the steady state with the accuracy of 0.08%. Namely, the maximum relative error between the computed and exact solution was 0.000778.

Fig. 3 shows a comparison between the computed (blue) and the exact solution (red) for the axial velocity (left), fluid pressure (middle), and radial displacement (right), showing excellent agreement. The corresponding relative errors are given by the following:

$$\frac{\|\mathbf{u}^e - \mathbf{u}\|_{L^2(\Omega^f)}}{\|\mathbf{u}^e\|_{L^2(\Omega^f)}} = 7.78 \times 10^{-4}, \qquad \frac{\|p^e - p\|_{L^2(\Omega^f)}}{\|p^e\|_{L^2(\Omega^f)}} = 1.17 \times 10^{-4},$$
$$\frac{\|\eta_r^e - \eta_r\|_{L^2(0,L)}}{\|\eta_r^e\|_{L^2(0,L)}} = 3.82 \times 10^{-5}, \qquad \frac{\|d_r^e - d_r\|_{L^2(\Omega^s)}}{\|d_r^e\|_{L^2(\Omega^s)}} = 3.82 \times 10^{-5}.$$

We conclude that the scheme behaves well for this simplified FSI problem with multiple structural layers.

6.2. Numerical Example 2: a fully nonlinear FSI problem

In this example we solved a full, nonlinear FSI problem (1)–(16) with the structure consisting of two layers, one with thickness h (thin) and one with thickness $H > h$ (thick). The combined thickness of the composite structure was $h + H = 0.12$ cm. The data and parameters used in the simulation are given in Table 2.

The elastodynamics of the thin structural layer was modeled by the Koiter membrane equations (6), (7), while the elastodynamics of the thick structure by the equations of 2D linear elasticity (9). The fluid flow is driven by the time-dependent pressure data:

$$p_{in}(t) = \begin{cases} \frac{p_{max}}{2}\left[1 - \cos\left(\frac{2\pi t}{t_{max}}\right)\right] & \text{if } t \le t_{max} \\ 0 & \text{if } t > t_{max} \end{cases}, \quad p_{out}(t) = 0 \; \forall t \in (0, T),$$

where $p_{max} = 1.333 \times 10^4$ (dyne/cm^2) and $t_{max} = 0.003$ (s). The corresponding (local) Reynold's number is 284.

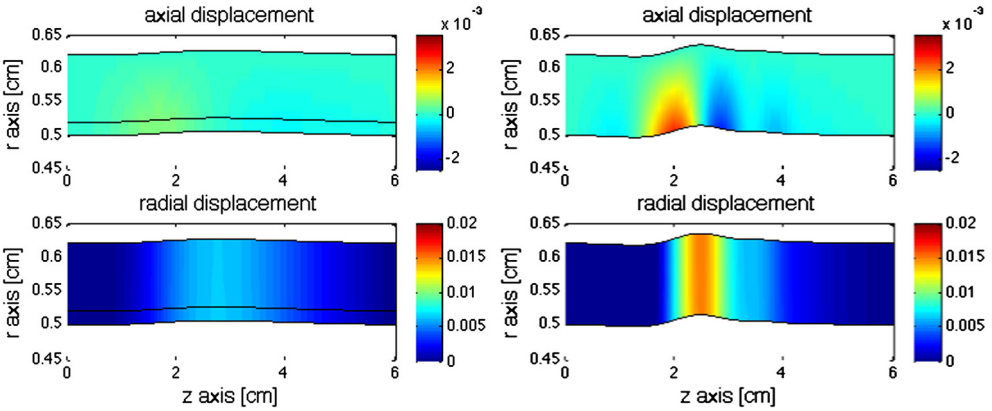

Fig. 4. Axial displacement (top) and radial displacement (bottom) at time $t = 8$ ms obtained using the model capturing two structural layers (left), and the model capturing FSI with a single thick structural layer [13] (right).

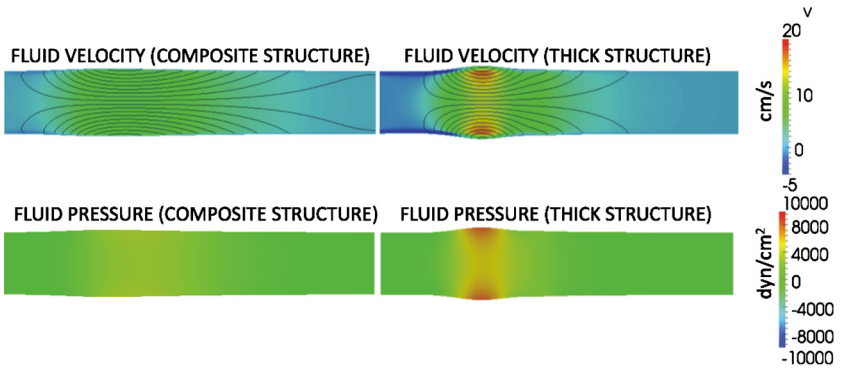

Fig. 5. Fluid velocity (top) and fluid pressure (bottom) at time $t = 8$ ms obtained using the model capturing two structural layers (left), and the model capturing FSI with a single thick structural layer [13] (right).

We simulated a sequence of FSI problems (1)–(16) for different values of the thicknesses h of the thin structure. Since there are no benchmark results related to FSI with composite structures, we studied the behavior of solutions as h converges to zero, and compared the limiting solution with a known benchmark solution of a FSI problem containing only a single thick structural layer. As $h \to 0$ we let the combined thickness $h + H$ of the structure remain fixed, and equal to 0.12 cm. We show below that the limiting solution as $h \to 0$, obtained using the solver presented in this manuscript with $\beta = 1$, is in excellent agreement with the solution of the FSI problem containing a single thick structure with thickness $H = 0.12$ cm, which was obtained using a different computational solver, namely the solver developed in [13].

Both problems were solved over the time interval $[0, 0.012]$ s, using the time step $\Delta t = 5 \times 10^{-5}$. The spatial discretization was performed using P1-iso-P2 elements for the fluid problem on a mesh containing 341×15 fluid nodes, while the structure problem was approximated using P1 elements on a mesh containing 341×7 nodes. Fig. 4 shows the axial and radial displacement at time $t = 8$ ms obtained using the multilayered model (left) with $h > 0$, and the single-layered model (right). Fig. 5 shows the corresponding fluid velocity and pressure. One can notice significant smoothing of both the displacement as well as the fluid velocity and pressure in the composite, i.e., multi-layered structure case. Same data was used for both simulations.

We then decreased h and increased H to maintain the constant combined thickness $h + H = 0.12$ cm, to obtain the results in Figs. 6, 7 and 8. Shown are the flowrate, mean pressure and displacement of the fluid–structure interface obtained using different values of h. We can see that as we decrease the thickness of the fluid–structure interface (from $h = 0.02$ to $h = 0.0025$), the numerical results obtained using our multilayered model, approach the results obtained using the single-layered FSI model, labeled with $h = 0$. Notice how for $h = 0.0025$ cm the solutions obtained using the multilayered model and the single thick structure model ($h = 0$ in Figs. 6, 7, 8) are almost identical.

We conclude this section by showing the log–log plots of computational error versus time and space discretization steps, presented in Figs. 9 and 10. The red line in the plots indicates the slope associated with the 1st-order accuracy. We see that our computational solver is 1st-order accurate in both time and space for the structure displacement calculations. We observe the higher order temporal and spatial accuracy for the fluid velocity, while fluid pressure exhibits the first order accuracy in space and the higher order accuracy in time.

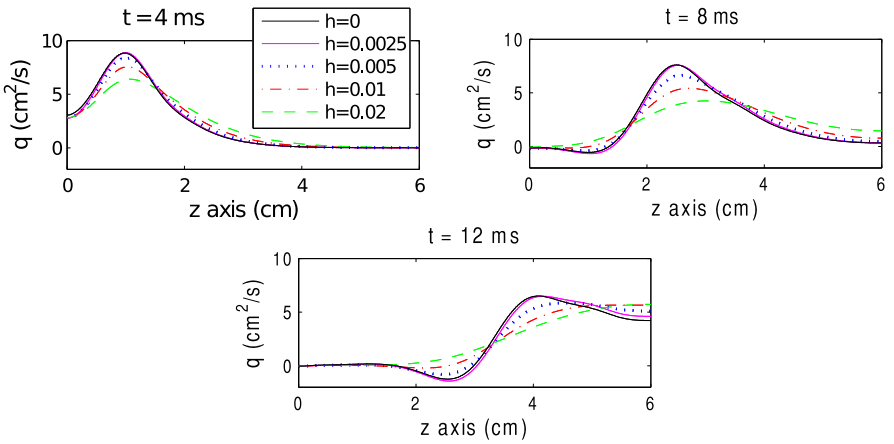

Fig. 6. The flowrate computed using two different models: the model in [13] containing a single thick structural layer ($h = 0$), and the model considered in this manuscript, consisting of two layers. The thickness of the thin membrane layer was decreased from $h = 0.02$ to $h = 0.0025$ cm. The combined thickness of the two-layered composite structure was kept constant at $h + H = 0.12$ cm. Convergence of the solutions to the FSI solution containing a single, thick structure ($h = 0$) can be observed.

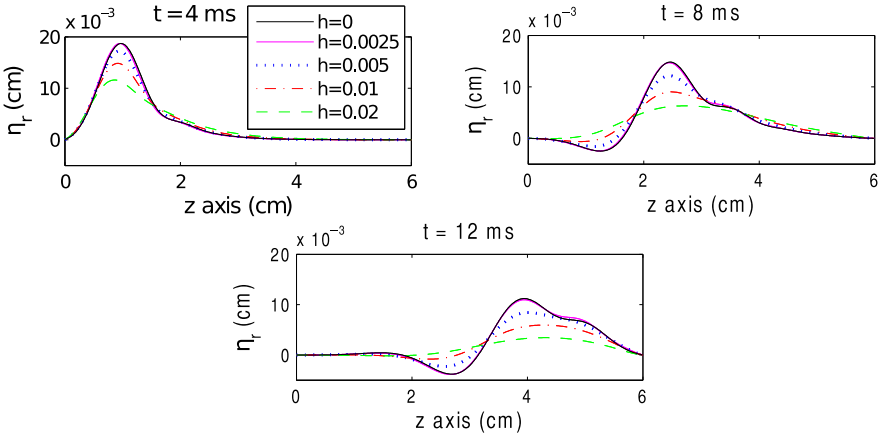

Fig. 7. Displacement of the fluid–structure interface obtained under the same conditions as those described in Fig. 6.

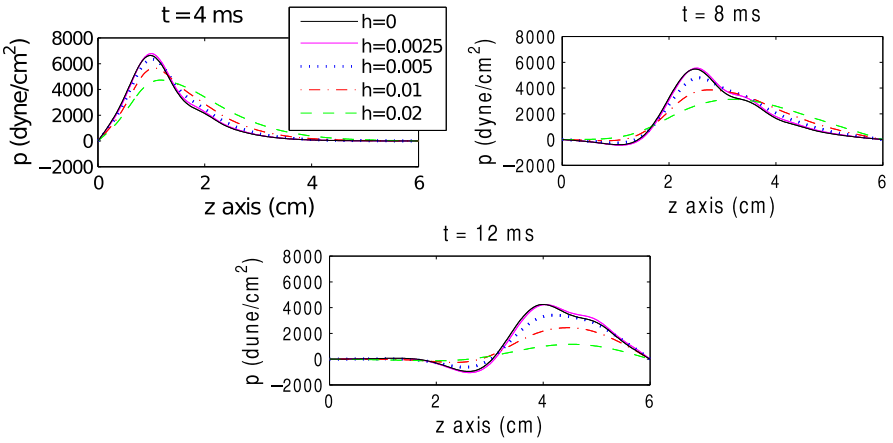

Fig. 8. Mean pressure obtained under the same conditions as those described in Fig. 6.

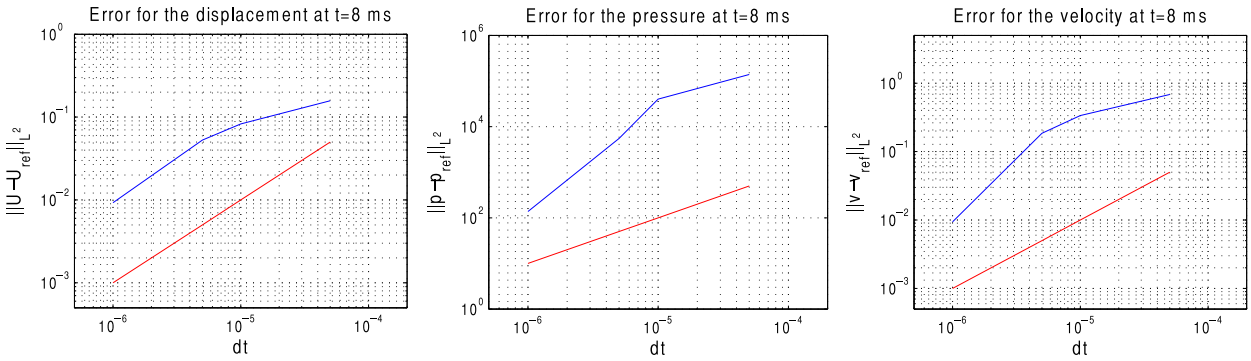

Fig. 9. Temporal accuracy: The figure shows the log–log plots of the L^2-error for the structure displacement, fluid pressure and velocity vs. time step. The red line shows the slope associated with first-order accuracy. We see 1st-order accuracy for displacement, and higher-order accuracy for the pressure and velocity. (For interpretation of the references to color in this figure legend, the reader is referred to the web version of this article.)

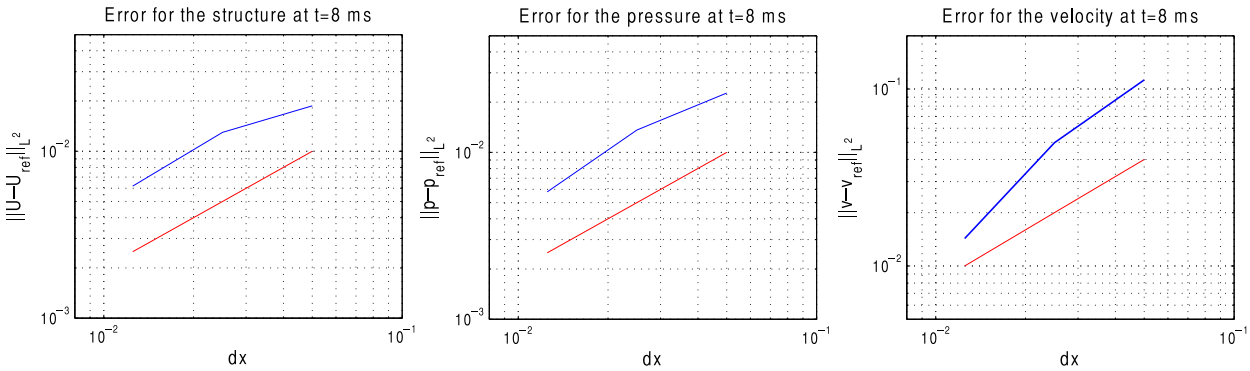

Fig. 10. Spatial accuracy: The figure shows the log–log plots of the L^2-error for the structure displacement, fluid pressure and velocity vs. spatial discretization step. The red line shows the slope associated with first-order accuracy. We observe 1st-order accuracy in displacement and pressure, and higher-order accuracy for the velocity. (For interpretation of the references to color in this figure legend, the reader is referred to the web version of this article.)

In this benchmark problem, we impose a large inlet pressure during the first $3 \cdot 10^{-3}$ s, after which the pressure wave propagates until it reaches the end of the tube at time $T = 12 \cdot 10^{-3}$ s. In order to capture the physics of this problem, the largest time step we consider is $\Delta t = 10^{-4}$. Even in this case, the total energy of the problem remains bounded by the inlet data.

6.3. Regularizing effects by thin fluid–structure interface with mass

In this manuscript we hypothesize for the first time that a fluid–structure interface with mass regularizes solutions of FSI problems between an incompressible, viscous fluid and an elastic structure. Namely, we hypothesize that the results presented in Figs. 6, 7, 8 depicting smoothed out solutions in the case when $h > 0$ reflecting the presence of a fluid–structure interface with inertia, are not a consequence of a numerical solver, but rather a property of the mathematical (physical) problem itself. We support this hypothesis by: (1) studying the displacement and displacement velocity of the fluid–structure interface to measure the effects of inertia, and (2) discussing a related analytical result supporting the regularization hypothesis of fluid–structure interface with mass.

Indeed, in Fig. 11, the first row shows three snap-shots of the fluid–structure interface as the pressure wave travels down the tube. In the second row of Fig. 11 the same three snap-shots are shown depicting the fluid–structure interface velocity. The red solid line in these figures corresponds to the massless fluid–structure interface in the FSI problem with a single thick structural layer. The black dashed line corresponds to the fluid–structure interface with mass in the FSI problem with two structural layers. We see significant damping of the traveling wave in the case when the fluid–structure interface has mass. This indicates that the inertia of the fluid–structure interface with mass regularizes solutions of FSI problems.

Similar issues were studied from the analysis point of view in the work by Hansen and Zuazua [39] in which it was shown that the presence of point mass at the interface between two linearly elastic strings smooths out the solution of this simplified FSI problem. In particular, in [39] two linearly elastic strings were considered, meeting at a point mass. The elastodynamics of each string was modeled by the 1D linear wave equation. It was shown that as the wave with the displacement in $H^1(0, L)$ and velocity in $L^2(0, L)$ passes through the point mass, the transmitted wave gets smoothed out to an $H^2(0, L)$ function, with velocity in $H^1(0, L)$. A numerical simulation of this phenomenon was presented in [49], and is shown here in Fig. 12. Notice how the transmitted wave in the panel on the right has higher regularity (a smoothed out

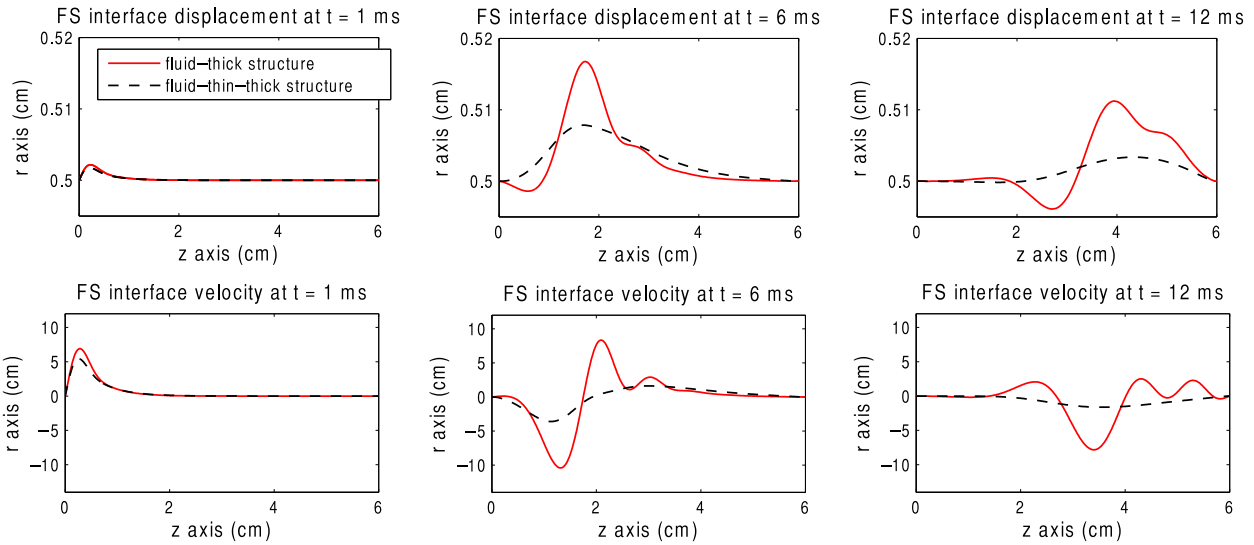

Fig. 11. Fluid–structure interface displacement (top) and velocity (bottom) obtained using the multilayered wall model discussed in the present manuscript, and the single layered model from [13], shown at times $t = 1$ ms, $t = 6$ ms, and $t = 12$ ms.

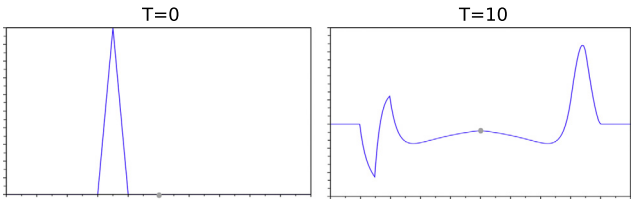

Fig. 12. Regularizing effects of point mass. The figure is taken from [49]. The initial data (left panel) is smoothed out as the transmitted wave traveling to the right, passes through the point mass (right panel).

tip of the wave) than the reflected wave on the left side in this figure. For a reader with further interest in this area we mention [43,71,76].

7. Conclusions

The focus of this manuscript was on fluid–structure interaction with composite structures. The benchmark problem proposed here was motivated by applications in hemodynamics. A stable, loosely-coupled partitioned scheme, based on the time-discretization via Lie operator splitting was proposed to numerically solve the underlying problem. An energy estimate was derived for the fully nonlinear moving-boundary problem, showing unconditional stability of the scheme for $\beta = 0$. Numerical results show that the scheme is stable and convergent for other values of $\beta \in [0, 1]$.

Particular attention was paid to a multi-physics FSI problem in which the structure is composed of two layers: a thin elastic layer with inertia which is in contact with the fluid, and a thick layer which sits on top of the thin layer. The thin layer serves as a fluid–structure interface with mass. The presence of the thin fluid–structure interface with mass has profound consequences both on the numerical implementation of the scheme, and on the physical properties of solutions to this problem. It allows full decoupling between the fluid and structure sub-solvers, and it serves as a regularizing mechanism for solutions of FSI problem. In contrast with FSI problems with massless interfaces, such as FSI problems with only thick structures, the fluid–structure interface with mass allows a more efficient energy dissipation, which gives rise to damping in the amplitude of structural waves, as well as the entire solution.

This is the first study which reports on the damping effects of fluid–structure interfaces with mass. Further research related to the precise theoretical quantification of this effect is under way, see e.g., [59] for the 1D heat-wave problems.

Acknowledgements

The authors would like to thank the reviewers for the careful reading of the manuscript and for the many suggestions which improved the final quality of the manuscript. Research of Bukač was partially supported by NSF via grant DMS-1318763. Research of Čanić was partially supported by NSF via grants NIGMS DMS-1263572, DMS-1318763, DMS-1311709, DMS-1262385 and DMS-1109189. Research of Muha was partially supported by NSF via grant DMS-1311709.

Appendix A. Proof of convergence as $h \to 0$ of FSI solutions with composite structures to a FSI solution with a single thick structure

We consider here the original FSI problem (1)–(16) satisfying the following simplifying assumptions:

1. The fluid problem is defined on a fixed fluid domain Ω^f (linear coupling).
2. Fluid advection is neglected leading to a time-dependent Stokes problem for the fluid.

In this case the coupled FSI problem with composite structure consisting of a thick structure sitting on top of a thin membrane with thickness h, serving as a fluid–structure interface with mass, takes the following form:

$$\left.\begin{aligned} &\varrho_f \partial_t \boldsymbol{v}^h = \nabla \cdot \boldsymbol{\sigma}^f\left(\boldsymbol{v}^h, p^h\right) \\ &\nabla \cdot \boldsymbol{v}^h = 0 \end{aligned}\right\} \quad \text{in } \Omega^f \times (0,T), \tag{48}$$

$$\rho_s \partial_t^2 \boldsymbol{U}^h + \gamma \boldsymbol{U}^h = \nabla \cdot \boldsymbol{\sigma}^s\left(\boldsymbol{U}^h\right) \quad \text{in } \Omega^s \times (0,T), \tag{49}$$

$$\left.\begin{aligned} &\rho_m h \partial_t^2 \eta_z^h - C_2(h)\partial_z \eta_r^h - C_1(h)\partial_z^2 \eta_z^h = -\boldsymbol{\sigma}^f \mathbf{n}\cdot\mathbf{e}_z + S\mathbf{n}\cdot\mathbf{e}_z \\ &\rho_m h \partial_t^2 \eta_r^h + C_0(h)\eta_r^h + C_2(h)\partial_z \eta_z^h = -\boldsymbol{\sigma}^f \mathbf{n}\cdot\mathbf{e}_r + S\mathbf{n}\cdot\mathbf{e}_r \\ &\boldsymbol{v}^h = \partial_t \boldsymbol{\eta}^h \end{aligned}\right\} \quad \text{on } \Gamma \times (0,T), \tag{50}$$

$$\boldsymbol{\sigma}\boldsymbol{n}_{in}^f = -p_{in}(t)\boldsymbol{n}_{in}^f \quad \text{on } \Gamma_{in}^f \times (0,T), \tag{51}$$

$$\boldsymbol{\sigma}\boldsymbol{n}_{out}^f = -p_{out}(t)\boldsymbol{n}_{out}^f \quad \text{on } \Gamma_{out}^f \times (0,T), \tag{52}$$

where the coefficients $C_i(h)$, $i = 0,1,2$, all depend on h and are given by formulas (8). The super-script h in $\boldsymbol{v}^h$ refers to a solution of the FSI problem with composite structure in which h denotes the thickness of the fluid–structure interface with mass. Eqs. (48)–(52) are supplemented with initial and boundary data. This gives rise to a well-defined *linear* FSI problem.

The weak formulation of problem (48)–(52) is given by:

$$\begin{aligned} &-\varrho_f \int_0^T\!\!\int_{\Omega^f} \boldsymbol{v}^h \cdot \partial_t \boldsymbol{\varphi} + 2\mu_f \int_0^T\!\!\int_{\Omega^f} \mathbf{D}\left(\boldsymbol{v}^h\right) : \mathbf{D}(\boldsymbol{\varphi}) - \varrho_m h \int_0^T\!\!\int_{\Gamma} \partial_t \eta_r^h \partial_t \zeta_r \\ &\quad - \varrho_m h \int_0^T\!\!\int_{\Gamma} \partial_t \eta_z^h \partial_t \zeta_z + C_2(h) \int_0^T\!\!\int_{\Gamma} \left(\partial_z \eta_z^h \zeta_r - \partial_z \eta_r^h \zeta_z\right) + C_1(h) \int_0^T\!\!\int_{\Gamma} \partial_z \eta_z^h \partial_z \zeta_z \\ &\quad + C_0(h) \int_0^T\!\!\int_{\Gamma} \eta_r^h \zeta_r - \varrho_s \int_0^T\!\!\int_{\Omega_s} \partial_t \mathbf{U}^h \cdot \partial_t \boldsymbol{\psi} + 2\mu_s \int_0^T\!\!\int_{\Omega^s} \boldsymbol{D}\left(\boldsymbol{U}^h\right) : \boldsymbol{D}(\boldsymbol{\psi}) + \lambda_s \int_{\Omega^s} \left(\nabla \cdot \boldsymbol{U}^h\right)(\nabla \cdot \boldsymbol{\psi}) + \gamma \int_0^T\!\!\int_{\Omega^s} \boldsymbol{U}^h \cdot \boldsymbol{\psi} \\ &= \pm \int_0^T\!\!\int_{\Gamma_{in/out}^f} p_{in/out}(t)\varphi_z + \rho_f \int_{\Omega^f} \boldsymbol{v}_0 \cdot \boldsymbol{\varphi}(0) + \rho_m h \int_{\Gamma} \partial_t \boldsymbol{\eta}(0)\boldsymbol{\zeta}(0) + \rho_s \int_{\Omega^s} \mathbf{V}_0 \cdot \boldsymbol{\psi}(0), \end{aligned} \tag{53}$$

for all $(\boldsymbol{\varphi}, \boldsymbol{\zeta}, \boldsymbol{\psi}) \in C_c^1(0,T; V^f(\Omega^f) \times H_0^1(0,L)^2 \times U^s(\Omega^s))$, such that $\boldsymbol{\varphi}|_{\Gamma} = \boldsymbol{\zeta} = \boldsymbol{\psi}|_{\Gamma}$, where

$$V^f = \left\{\boldsymbol{\varphi} \in H^1\left(\Omega^f\right)^2 \;\middle|\; \varphi_r|_{r=0} = 0,\ \boldsymbol{\varphi}|_{z=0,L} = 0\right\},$$

$$U^s = \left\{\boldsymbol{\varphi} \in H^1\left(\Omega^s\right)^2 \;\middle|\; \psi_z|_{\Gamma_{ext}} = 0,\ \boldsymbol{\psi}|_{z=0,L} = 0\right\},$$

and $C_0(h)$, $C_1(h)$, and $C_2(h)$ are given by (8).

It is easy to see that for every $h > 0$ there exists a weak solution $(\boldsymbol{v}^h, \boldsymbol{\eta}^h, \mathbf{U}^h)$ to problem (48)–(52) satisfying the following energy inequality:

$$\begin{aligned} &\varrho_f \left\|\boldsymbol{v}^h\right\|^2_{L^\infty([0,T);L^2(\Omega^f))} + \mu_f \left\|\mathbf{D}\left(\boldsymbol{v}^h\right)\right\|^2_{L^2(0,T;L^2(\Omega^f))} + \varrho_m h \left\|\partial_t \boldsymbol{\eta}^h\right\|^2_{L^\infty(0,T;L^2(\Gamma))} \\ &\quad + h\left(4\mu_m \left\|\frac{\eta_r^h}{R}\right\|^2_{L^2(0,L)} + 4\mu_m \left\|\partial_z \eta_z^h\right\|^2_{L^2(0,L)} + \frac{4\mu_m\lambda_m}{\lambda_m + 2\mu_m}\left\|\partial_z \eta_z^h + \frac{\eta_r^h}{R}\right\|^2_{L^2(0,L)}\right) \\ &\quad + \varrho_s \left\|\partial_t \mathbf{U}^h\right\|^2_{L^\infty(0,T;L^2(\Omega^s))} + C(\mu_s, \lambda_s, \gamma)\left\|\mathbf{U}^h\right\|^2_{L^2(0,T;H^1(\Omega^s))} \\ &\quad \le C(P_{in}, P_{out}, \boldsymbol{v}_0, \mathbf{V}_0, \eta_0). \end{aligned} \tag{54}$$

Since the right hand side of this energy inequality does not depend on h, the sequence of solutions of problems (48)–(52), defined for different values of h, is uniformly bounded. From here, the following weak and weak* convergence results hold as $h \to 0$:

$$\begin{aligned}
&\boldsymbol{v}^h \rightharpoonup \boldsymbol{v} \quad \text{weak}^* \text{ in } L^\infty\big(0,T;L^2(\Omega^f)\big),\\
&\boldsymbol{v}^h \rightharpoonup \boldsymbol{v} \quad \text{weak in } L^2\big(0,T;H^1(\Omega^f)\big),\\
&\mathbf{U}^h \rightharpoonup \mathbf{U} \quad \text{weak in } L^2\big(0,T;H^1(\Omega^s)\big),\\
&\partial_t\mathbf{U}^h \rightharpoonup \partial_t\mathbf{U} \quad \text{weak}^* \text{ in } L^\infty\big(0,T;L^2(\Omega^s)\big),\\
&\sqrt{h}\boldsymbol{\eta}^h \rightharpoonup \boldsymbol{\eta} \quad \text{weak in } L^2\big(0,T;L^2(\Gamma)\big)^2,\\
&\sqrt{h}\,\partial_t\boldsymbol{\eta}^h \rightharpoonup \boldsymbol{\eta}_1 \quad \text{weak}^* \text{ in } L^\infty\big(0,T;L^2(\Gamma)\big)^2,\\
&\sqrt{h}\,\partial_z\eta_z^h \rightharpoonup \eta_2 \quad \text{weak}^* \text{ in } L^\infty\big(0,T;L^2(\Gamma)\big).
\end{aligned} \tag{55}$$

From the uniqueness of the limit in $\mathcal{D}'(\Gamma)$ we conclude that $\boldsymbol{\eta}_1 = \partial_t\boldsymbol{\eta}$, and $\eta_2 = \partial_z\eta_z$.

What is left is to identify the limits $\boldsymbol{\eta}$ and $\partial_t\boldsymbol{\eta}$. From the kinematic coupling condition and the Trace Theorem we have:

$$\big\|\partial_t\boldsymbol{\eta}^h\big\|_{L^2([0,T);L^2(\Gamma))} = \big\|\boldsymbol{v}^h\big\|_{L^2(0,T;L^2(\Gamma))} \le \big\|\boldsymbol{v}^h\big\|_{L^2(0,T;H^1(\Omega^f))} \le C,$$

where C is independent of h. From the uniform boundedness of $\|\partial_t\boldsymbol{\eta}^h\|_{L^2(0,T;L^2(\Gamma))}$ we have

$$\sqrt{h}\partial_t\boldsymbol{\eta}^h \to 0 \quad \text{in } L^2\big(0,T;L^2(\Gamma)\big).$$

Uniqueness of the limit in $\mathcal{D}'(\Gamma)$ implies $\partial_t\boldsymbol{\eta} = 0$. Similarly, we get $\boldsymbol{\eta} = 0$ using the fact that $\boldsymbol{\eta}^h(s,.) = \eta_0 + \int_0^s \boldsymbol{\vartheta}_t\eta^h$.

We can now pass to the limit as $h \to 0$ in the linear problem (53)–(52) by using (55) to get the following equality:

$$\begin{aligned}
&-\varrho_f\int_0^T\!\!\int_{\Omega^f} \boldsymbol{v}\cdot\partial_t\boldsymbol{\varphi} + 2\mu_f\int_0^T\!\!\int_{\Omega^f}\mathbf{D}(\boldsymbol{v}):\mathbf{D}(\boldsymbol{\varphi}) - \varrho_s\int_0^T\!\!\int_{\Omega_s}\partial_t\mathbf{U}\cdot\partial_t\boldsymbol{\psi}\\
&\quad + 2\mu_s\int_0^T\!\!\int_{\Omega^s}\boldsymbol{D}(\boldsymbol{U}):\boldsymbol{D}(\boldsymbol{\psi}) + \lambda_s\int_{\Omega^s}(\nabla\cdot\boldsymbol{U})(\nabla\cdot\boldsymbol{\psi}) + \gamma\int_0^T\!\!\int_{\Omega^s}\boldsymbol{U}\cdot\boldsymbol{\psi}\\
&\quad = \pm\int_0^T\int_{\Gamma^f_{in/out}} p_{in/out}(t)\varphi_z + \rho_f\int_\Gamma \boldsymbol{v}_0\boldsymbol{\zeta}(0) + \rho_s\int_{\Omega^s}\mathbf{V}_0\cdot\boldsymbol{\psi}(0),
\end{aligned} \tag{56}$$

for all $(\boldsymbol{\phi},\boldsymbol{\psi}) \in C_c^1([0,T);V^f(\Omega^f)\times U^s(\Omega^s))$ such that $\boldsymbol{\phi}|_\Gamma = \boldsymbol{\psi}|_\Gamma$. This shows that the limiting functions satisfy the weak form of the FSI with a single, thick elastic structure, coupled to the motion of an incompressible, viscous fluid via a mass-less fluid–structure interface.

Remark 2. We did not have to identify the limit $\boldsymbol{\eta}$ in order to pass to the limit. Namely, we have:

$$\varrho_m h\partial_t\boldsymbol{\eta}^h = \sqrt{\varrho_m h}\big(\sqrt{\varrho_m h}\partial_t\boldsymbol{\eta}^h\big) \rightharpoonup \sqrt{\varrho_m h}\partial_t\boldsymbol{\eta} = 0.$$

References

[1] M. Astorino, F. Chouly, M.A. Fernández, An added-mass free semi-implicit coupling scheme for fluid–structure interaction, C. R. Math. 347 (1–2) (2009) 99–104.

[2] M. Astorino, F. Chouly, M.A. Fernández Varela, Robin based semi-implicit coupling in fluid–structure interaction: stability analysis and numerics, SIAM J. Sci. Comput. 31 (2009) 4041–4065.

[3] F.P.T. Baaijens, A fictitious domain/mortar element method for fluid–structure interaction, Int. J. Numer. Methods Fluids 35 (7) (2001) 743–761.

[4] S. Badia, F. Nobile, C. Vergara, Fluid–structure partitioned procedures based on Robin transmission conditions, J. Comput. Phys. 227 (2008) 7027–7051.

[5] S. Badia, F. Nobile, C. Vergara, Robin–Robin preconditioned Krylov methods for fluid–structure interaction problems, Comput. Methods Appl. Mech. Eng. 198 (33–36) (2009) 2768–2784.

[6] S. Badia, A. Quaini, A. Quarteroni, Splitting methods based on algebraic factorization for fluid–structure interaction, SIAM J. Sci. Comput. 30 (4) (2008) 1778–1805.

[7] A.T. Barker, X.C. Cai, Scalable parallel methods for monolithic coupling in fluid–structure interaction with application to blood flow modeling, J. Comput. Phys. 229 (3) (2010) 642–659.

[8] Y. Bazilevs, V.M. Calo, T.J.R. Hughes, Y. Zhang, Isogeometric fluid–structure interaction: theory algorithms and computations, Comput. Mech. 43 (2008) 3–37.

[9] Y. Bazilevs, V.M. Calo, Y. Zhang, T.J.R. Hughes, Isogeometric fluid–structure interaction analysis with applications to arterial blood flow, Comput. Mech. 38 (4–5) (2006) 310–322.

[10] M. Bukač, S. Čanić, R. Glowinski, J. Tambača, A. Quaini, Fluid–structure interaction in blood flow capturing non-zero longitudinal structure displacement, J. Comput. Phys. 235 (2013) 515–541.
[11] M. Bukač, P. Zunino, I. Yotov, An operator splitting approach for the interaction between a fluid and a multilayered poroelastic structure, to appear in Numer. Methods Partial Differ. Equ.
[12] M. Bukač, S. Čanić, Longitudinal displacement in viscoelastic arteries: a novel fluid–structure interaction computational model, and experimental validation, J. Math. Biosci. Eng. 10 (2) (2013) 258–388.
[13] M. Bukač, S. Čanić, R. Glowinski, B. Muha, A. Quaini, A modular, operator splitting scheme for fluid–structure interaction problems with thick structures, Int. J. Numer. Methods Fluids (2013), in press.
[14] E. Burman, M.A. Fernández, Stabilization of explicit coupling in fluid–structure interaction involving fluid incompressibility, Comput. Methods Appl. Mech. Eng. 198 (2009) 766–784.
[15] P. Causin, J.F. Gerbeau, F. Nobile, Added-mass effect in the design of partitioned algorithms for fluid–structure problems, Comput. Methods Appl. Mech. Eng. 194 (42–44) (2005) 4506–4527.
[16] G.H. Cottet, E. Maitre, T. Milcent, Eulerian formulation and level set models for incompressible fluid–structure interaction, Modél. Math. Anal. Numér. 42 (2008) 471–492.
[17] S. Deparis, M. Discacciati, G. Fourestey, A. Quarteroni, Fluid–structure algorithms based on Steklov–Poincaré operators, Comput. Methods Appl. Mech. Eng. 195 (41–43) (2006) 5797–5812.
[18] S. Deparis, M. Fernandez, L. Formaggia, Acceleration of a fixed point algorithm for a fluid–structure interaction using transpiration condition, Math. Model. Numer. Anal. 37 (4) (2003) 601–616.
[19] J. Donea, Arbitrary Lagrangian–Eulerian finite element methods, in: Computational Methods for Transient Analysis, North-Holland, Amsterdam, 1983.
[20] H. Fang, Z. Wang, Z. Lin, M. Liu, Lattice Boltzmann method for simulating the viscous flow in large distensible blood vessels, Phys. Rev. E 65 (5) (2002) 051925-1, 12 pp.
[21] C. Farhat, P. Geuzaine, C. Grandmont, The discrete geometric conservation law and the nonlinear stability of ale schemes for the solution of flow problems on moving grids, J. Comput. Phys. 174 (2) (2001) 669–694.
[22] L.J. Fauci, R. Dillon, Biofluidmechanics of reproduction, Ann. Rev. Fluid Mech. 38 (2006) 371–394.
[23] Z.G. Feng, E.E. Michaelides, The immersed boundary–lattice Boltzmann method for solving fluid–particles interaction problems, J. Comput. Phys. 195 (2) (2004) 602–628.
[24] M.A. Fernández, M. Moubachir, A Newton method using exact jacobians for solving fluid–structure coupling, Comput. Struct. 83 (2–3) (2005) 127–142.
[25] M.A. Fernández, Incremental displacement-correction schemes for the explicit coupling of a thin structure with an incompressible fluid, C. R. Math. Acad. Sci. Paris 349 (7–8) (2011) 473–477.
[26] M.A. Fernández, Incremental displacement-correction schemes for incompressible fluid–structure interaction: stability and convergence analysis, Numer. Math. 123 (2012) 210–265.
[27] M.A. Fernández, J.F. Gerbeau, C. Grandmont, A projection algorithm for fluid–structure interaction problems with strong added-mass effect, C. R. Math. 342 (4) (2006) 279–284.
[28] M.A. Fernández, J. Mullaert, Displacement-velocity correction schemes for incompressible fluid–structure interaction, C. R. Math. Acad. Sci. Paris 349 (17–18) (2011) 1011–1015.
[29] C.A. Figueroa, I.E. Vignon-Clementel, K.E. Jansen, T.J.R. Hughes, C.A. Taylor, A coupled momentum method for modeling blood flow in three-dimensional deformable arteries, Comput. Methods Appl. Mech. Eng. 195 (41–43) (2006) 5685–5706.
[30] A.L. Fogelson, R.D. Guy, Platelet-wall interactions in continuum models of platelet thrombosis: formulation and numerical solution, Math. Med. Biol. 21 (2004) 293–334.
[31] L. Formaggia, J.F. Gerbeau, F. Nobile, A. Quarteroni, On the coupling of 3d and 1d Navier–Stokes equations for flow problems in compliant vessels, Comput. Methods Appl. Mech. Eng. 191 (6–7) (2001) 561–582.
[32] J. Gerbeau, M. Vidrascu, A quasi-Newton algorithm based on a reduced model for fluid–structure interactions problems in blood flows, Math. Model. Numer. Anal. 37 (4) (2003) 631–648.
[33] R. Glowinski, Finite element methods for incompressible viscous flow, in: P.G. Ciarlet, J.-L. Lions (Eds.), Handbook of Numerical Analysis, vol. 9, North-Holland, Amsterdam, 2003.
[34] B.E. Griffith, Immersed boundary model of aortic heart valve dynamics with physiological driving and loading conditions, Int. J. Numer. Methods Biomed. Eng. 28 (3) (2012) 317–345.
[35] B.E. Griffith, On the volume conservation of the immersed boundary method, Commun. Comput. Phys. 12 (2) (2012) 401–432.
[36] B.E. Griffith, R.D. Hornung, D.M. McQueen, C.S. Peskin, An adaptive, formally second order accurate version of the immersed boundary method, J. Comput. Phys. 223 (1) (2007) 10–49.
[37] B.E. Griffith, R. Luo, D.M. McQueen, C.S. Peskin, Simulating the fluid dynamics of natural and prosthetic heart valves using the immersed boundary method, Int. J. Appl. Mech. 1 (2009) 137–177.
[38] G. Guidoboni, R. Glowinski, N. Cavallini, S. Čanić, Stable loosely-coupled-type algorithm for fluid–structure interaction in blood flow, J. Comput. Phys. 228 (18) (2009) 6916–6937.
[39] S. Hansen, E. Zuazua, Exact controllability and stabilization of a vibrating string with an interior point mass, SIAM J. Control Optim. 33 (5) (1995) 1357–1391.
[40] M. Heil, An efficient solver for the fully coupled solution of large-displacement fluid–structure interaction problems, Comput. Methods Appl. Mech. Eng. 193 (1–2) (2004) 1–23.
[41] T.J.R. Hughes, W.K. Liu, T.K. Zimmermann, Lagrangian–Eulerian finite element formulation for incompressible viscous flows, Comput. Methods Appl. Mech. Eng. 29 (3) (1981) 329–349.
[42] A. Hundertmark-Zaušková, M. Lukáčová-Medvid'ová, G. Rusnáková, Fluid–structure interaction for shear-dependent non-Newtonian fluids, in: Topics in Mathematical Modeling and Analysis, in: Jindřich Nečas Cent. Math. Model. Lect. Notes, vol. 7, Matfyzpress, Prague, 2012, pp. 109–158.
[43] M. Koch, E. Zuazua, A hybrid system of PDE's arising in multi-structure interaction: coupling of wave equations in n and $n-1$ space dimensions, in: Recent Trends in Partial Differential Equations, in: Contemp. Math., vol. 409, Amer. Math. Soc., Providence, RI, 2006, pp. 55–77.
[44] M. Krafczyk, M. Cerrolaza, M. Schulz, E. Rank, Analysis of 3D transient blood flow passing through an artificial aortic valve by lattice-Boltzmann methods, J. Biomech. 31 (5) (1998) 453–462.
[45] M. Krafczyk, J. Tölke, E. Rank, M. Schulz, Two-dimensional simulation of fluid–structure interaction using lattice-Boltzmann methods, Comput. Struct. 79 (22–25) (2001) 2031–2037.
[46] Young W. Kwon, Angela C. Owens, Dynamic responses of composite structures with fluid–structure interaction, in: B. Attaf (Ed.), Advances in Composite Materials – Ecodesign and Analysis, InTech Europe, ISBN 978-953-307-150-3, 2011, pp. 337–358.
[47] C.S. Peskin, L.A. Miller, A computational fluid dynamics study of 'clap and fling' in the smallest insects, J. Exp. Biol. 208 (2005) 195–212.
[48] P. Le Tallec, J. Mouro, Fluid structure interaction with large structural displacements, Comput. Methods Appl. Mech. Eng. 190 (24–25) (2001) 3039–3067.
[49] V. Lescarret, E. Zuazua, Numerical approximation schemes for multi-dimensional wave equations in asymmetric spaces, preprint.
[50] A. Leuprecht, K. Perktold, M. Prosi, T. Berk, W. Trubel, H. Schima, Numerical study of hemodynamics and wall mechanics in distal end-to-side anastomoses of bypass grafts, J. Biomech. 35 (2) (2002) 225–236.

[51] S. Lim, C.S. Peskin, Simulations of the whirling instability by the immersed boundary method, SIAM J. Sci. Comput. 25 (6) (2004) 2066–2083.
[52] M. Galindo, M. Cervera, R. Codina, On the computational efficiency and implementation of block-iterative algorithms for nonlinear coupled problems, Eng. Comput. 13 (1996) 4–30.
[53] A. Hundertmark-Zaušková, M. Lukáčová-Medvid'ová, G. Rusnáková, Kinematic splitting algorithm for fluid–structure interaction in hemodynamics, Comput. Methods Appl. Mech. Eng. 265 (2013) 83–106.
[54] X. Ma, G.C. Lee, S.G. Lu, Numerical simulation for the propagation of nonlinear pulsatile waves in arteries, ASME J. Biomech. Eng. 114 (1992) 490–496.
[55] H. Matthies, J. Steindorf, Numerical efficiency of different partitioned methods for fluid–structure interaction, Z. Angew. Math. Mech. 2 (80) (2000) 557–558.
[56] C. Michler, S.J. Hulshoff, E.H. van Brummelen, R.x de Borst, A monolithic approach to fluid–structure interaction, Comput. Fluids 33 (2004) 839–848.
[57] A. Mikelic, G. Guidoboni, S. Čanić, Fluid–structure interaction in a pre-stressed tube with thick elastic walls I: the stationary Stokes problem, Netw. Heterog. Media 2 (3) (2007) 397.
[58] L.A. Miller, C.S. Peskin, A computational fluid dynamics of 'clap and fling' in the smallest insects, J. Exp. Biol. 208 (2) (2005) 195–212.
[59] B. Muha, A note on optimal regularity and regularizing effects of point mass coupling for a heat-wave system, arXiv:1403.3965, 2014.
[60] B. Muha, S. Čanić, Existence of a weak solution to a fluid–structure interaction problem motivated by blood–artery–stent interaction, 2013, in preparation.
[61] B. Muha, S. Čanić, Existence of a weak solution to a nonlinear fluid–structure interaction problem modeling the flow of an incompressible, viscous fluid in a cylinder with deformable walls, Arch. Ration. Mech. Anal. 207 (3) (2013) 919–968.
[62] B. Muha, S. Čanić, Existence of a weak solution to a fluid-multi–layered-structure interaction problem, J. Differ. Equ. 256 (2014) 658–706.
[63] Boris Muha, Sunčica Čanić, A nonlinear, 3D fluid–structure interaction problem driven by the time-dependent dynamic pressure data: a constructive existence proof, Commun. Inf. Syst. 13 (3) (2013) 357–397.
[64] C.M. Murea, S. Sy, A fast method for solving fluid–structure interaction problems numerically, Int. J. Numer. Methods Fluids 60 (10) (2009) 1149–1172.
[65] F. Nobile, Numerical approximation of fluid–structure interaction problems with application to haemodynamics, PhD thesis, EPFL, Switzerland, 2001.
[66] F. Nobile, C. Vergara, An effective fluid–structure interaction formulation for vascular dynamics by generalized Robin conditions, SIAM J. Sci. Comput. 30 (2008) 731–763.
[67] C.S. Peskin, Numerical analysis of blood flow in the heart, J. Comput. Phys. 25 (3) (1977) 220–252.
[68] C.S. Peskin, D.M. McQueen, Modeling prosthetic heart valves for numerical analysis of blood flow in the heart, J. Comput. Phys. 37 (1) (1980) 113–132.
[69] A. Quaini, A. Quarteroni, A semi-implicit approach for fluid–structure interaction based on an algebraic fractional step method, Math. Models Methods Appl. Sci. 17 (6) (2007) 957–985.
[70] A. Quarteroni, M. Tuveri, A. Veneziani, Computational vascular fluid dynamics: problems, models and methods, Comput. Vis. Sci. 2 (4) (2000) 163–197.
[71] J. Rauch, X. Zhang, E. Zuazua, Polynomial decay for a hyperbolic–parabolic coupled system, J. Math. Pures Appl. (9) 84 (4) (2005) 407–470.
[72] R. Van Loon, P.D. Anderson, J. De Hart, F.P.T. Baaijens, A combined fictitious domain/adaptive meshing method for fluid–structure interaction in heart valves, Int. J. Numer. Methods Fluids 46 (5) (2004) 533–544.
[73] S. Čanić, D. Lamponi, A. Mikelić, J. Tambača, Self-consistent effective equations modeling blood flow in medium-to-large compliant arteries, Multiscale Model. Simul. 3 (3) (2005) 559–596.
[74] S. Čanić, B. Muha, M. Bukač, Stability of the kinematically coupled β-scheme for fluid–structure interaction problems in hemodynamics, Int. J. Numer. Anal. Model. (2014), arXiv:1205.6887, in press.
[75] Wikipedia, Composite materials, http://en.wikipedia.org/wiki/Composite_material, 2013.
[76] X. Zhang, E. Zuazua, Long-time behavior of a coupled heat-wave system arising in fluid–structure interaction, Arch. Ration. Mech. Anal. 184 (1) (2007) 49–120.
[77] S. Zhao, X. Xu, M. Collins, The numerical analysis of fluid–solid interactions for blood flow in arterial structures. Part 2: development of coupled fluid–solid algorithms, Proc. Inst. Mech. Eng., H 212 (1998) 241–252.